

Impact of adaptively thinned AIRS cloud-cleared radiances on tropical cyclone representation in a global data assimilation and forecast system

Oreste Reale* [†], Erica L. McGrath-Spangler [‡],

Will McCarty, Daniel Holdaway [§], Ronald Gelaro

Global Modeling and Assimilation Office, NASA, Greenbelt, Maryland, USA

*Corresponding author address: Oreste Reale, NASA Goddard Space Flight Center, Code 610.1, Greenbelt, MD 20771.

E-mail: oreste.reale-1@nasa.gov

[†]Universities Space Research Association, Goddard Earth Sciences Technology and Research, Columbia, Maryland, USA

[‡]Universities Space Research Association, Goddard Earth Sciences Technology and Research, Columbia, Maryland, USA

[§]Universities Space Research Association, Goddard Earth Sciences Technology and Research, Columbia, Maryland, USA

ABSTRACT

15 A simple adaptive thinning methodology for Atmospheric Infrared Sounder
16 (AIRS) radiances is evaluated through a combination of Observing System
17 Experiments (OSEs) and adjoint methodologies. The OSEs are performed
18 with the NASA Goddard Earth Observing System (GEOS, version 5) data as-
19 simulation and forecast model. In addition, the adjoint-based forecast sensitiv-
20 ity observation impact technique is applied to assess fractional contributions
21 of sensors in different thinning configurations. The adaptive strategy uses a
22 denser AIRS coverage in a moving domain centered around tropical cyclones
23 (TCs), sparser everywhere else. The OSEs consist of two sets of data assim-
24 ilation runs that cover the period from September 1st to 10 November 2014,
25 with the first 20 days discarded for spin-up. Both sets assimilate all conven-
26 tional and satellite observations used operationally. In addition, one ingests
27 clear-sky AIRS radiances, the other cloud-cleared radiances, each compris-
28 ing multiple thinning strategies. Daily 7-day forecasts are initialized from all
29 these analyses and evaluated with focus on TCs over the Atlantic and the Pa-
30 cific. Evidence is provided on the effectiveness of this simple TC-centered
31 adaptive radiance thinning strategy, in full agreement with previous theoret-
32 ical studies. Specifically, global skill increases, and tropical cyclone repre-
33 sentation is substantially improved. The improvement is particularly strong
34 when cloud-cleared radiances are assimilated. Finally, the article suggests
35 that cloud-cleared radiances, if thinned more aggressively than the currently
36 used clear-sky radiances, could successfully replace them with large improve-
37 ments in TC forecasting and no loss of global skill.

1. Introduction

a. Assimilation of AIRS radiances: stating the problems

Data from the Atmospheric Infrared Sounder (AIRS), onboard the NASA Aqua satellite, have been extensively used by operational weather forecasting centers worldwide for more than a decade. Evidence that the assimilation of AIRS radiances brought a positive impact on the European Centre for Medium-Range Weather Forecasts operational system was provided, among others, by McNally et al. (2006). Similarly, positive impact was shown for the National Centers for Environmental Prediction (NCEP) system (e.g., Chahine et al. 2006; Le Marshall et al. 2006). Over the following years, other hyperspectral instruments have been designed and placed into orbit: the Cross-track Infrared Sounder (CrIS) onboard the Suomi National Polar-orbiting Partnership (NPP), launched on 28 October 2011, and the two Infrared Atmospheric Sounding Interferometers (IASI), onboard the MetOp-A and MetOp-B satellites, launched on 19 October 2006 and 17 September 2012, respectively. The combined impact of infrared instruments appears to be dominant in current operational weather forecasting as shown, among others, by Joo et al. (2013) in their evaluation of IASI (MetOp-A) and AIRS in the UK Met Office system through adjoint methodologies. However, because the number of observations assimilated operationally per cycle is currently approaching 10^7 , it is becoming increasingly difficult for a single instrument to positively impact the forecast skill.

Aggressive data reduction algorithms are necessary because of computational cost but also for another, less immediate, reason: to reduce the effects of horizontally correlated errors. High data density, while intuitively desirable, increases the possibility of not satisfying the crucial assumption of errors being independent, which is a basic requirement in current operational data assimilation systems. Ochotta et al. (2005) clearly state that “*a high spatial and/or temporal data*

61 *density can severely violate the assumption of independent observation errors*'. Since the control
62 of error correlation between observations is an extraordinarily difficult problem, the large volume
63 of AIRS data and other infrared instruments is often suboptimally sampled on a regularly spaced
64 grid through the thinning procedure. This is in apparent contrast with the goals of instrument and
65 algorithm development teams, who are often focused on designing better products in terms of a
66 larger channel selection, larger data volume, and denser coverage.

67 In addition to suboptimal sampling, another fundamental limitation hinders the full exploitation
68 of AIRS and other infrared sensors: the limitation to the use of clear-sky radiances. Currently,
69 only data from channels that are thought to be unaffected by clouds are assimilated. This is in
70 contrast with the routine operational use of cloud-affected microwave radiances (e.g., Bauer et
71 al. 2010; Zhu et al. 2016), and poses a serious limitation to the usefulness of the infrared data,
72 since clear areas are meteorologically less active. From the point of view of tropical cyclone (TC)
73 forecasting, the rejection of cloud-contaminated channels often leaves evident data void areas
74 which are in marked correspondence to tropical cyclone circulations. This is particularly harmful
75 in cases in which no additional observations, such as the ones obtained by Hurricane Hunters'
76 flights, are available inside the storm's circulation (e.g. Reale et al. 2009b).

77 *b. The potential of adaptive thinning*

78 A reasonable agreement exists on the fact that assimilation of additional observations in regions
79 where the observational network is dense, initial conditions are accurately known, or where error
80 growth is small, can yield only modest or no forecast improvements (e.g., Morss et al. 2001). That
81 study, among others, convincingly argued that adaptive strategies, based on ingesting additional
82 observations from areas where observational errors are large, or where forecast errors grow more
83 rapidly, could be very effective. A vast number of adaptive strategies have been proposed, such

as techniques based on ensemble spread (e.g., Lorenz and Emanuel 1998), singular vectors (e.g., Gelaro et al. 1999), and ensemble transform techniques (e.g., Bishop and Toth 1999).

From the point of view of the present study, which is focused on assimilation of infrared radiances, particularly relevant is a seminal work by Liu and Rabier (2003, hereafter LR03) which discusses the potential of high-density observations in an Observing System Simulation Experiment (OSSE) four-dimensional variational (4DVAR) context. The major finding, confirming their previous, more theoretical, one-dimensional assessment (Liu and Rabier 2002), is that increased observation density with uncorrelated errors always increases the analysis accuracy. At the same time, LR03 found that an increase in observation density degrades both analysis and forecast if the error correlation between adjacent observations is greater than a certain threshold. Therefore, a separation between an optimal analysis, in which errors are uncorrelated, and a suboptimal analysis, in which errors are assumed to be uncorrelated while in reality they are, could be ideally achievable, based on an error correlation threshold.

Several methodologies, based on the conceptual understanding provided by LR03, were proposed in the following years. Among them, Ochotta et al. (2005) presented two thinning algorithms, called top-down clustering and estimation error analysis, to reduce the number of assimilated observations while retaining the essential information content of the data. This results in an observation density that is greater in rapidly changing regions. In Ochotta et al. (2007), a further improvement and revisitation of the estimation error analysis technique was provided. Bondarenko et al. (2007) presented a comprehensive discussion on the impact of observation density, and clarified the fundamental fact that a suboptimal analysis is often a necessary choice because of the difficulty and cost of determining observation-error correlations. Lazarus et al. (2010) provided an in-depth comparison of ‘standard’ (i.e., regularly gridded) against ‘intelligent’ (i.e., adaptive) thinning techniques, stating that ‘simple thinning tends to perform better over the relatively un-

108 interesting homogeneous data regions'. Unfortunately, in spite of the deep underlying theoretical
109 understanding and by the very convincing findings of the above referred studies, the difficulties
110 associated with the widespread operational implementation of adaptive methods have proven, so
111 far, insurmountable.

112 Therefore, in practice, most operational centers are still compelled to use a regularly spaced grid
113 to perform data thinning, simply assuming that errors are uncorrelated, even if they are not. The
114 Gridpoint Statistical Interpolation (GSI, Wu et al. 2002; Purser et al. 2003a, 2003b), which is
115 the foundation of the GEOS Data Assimilation System (DAS), is no exception. Satellite radiance
116 data, including AIRS data, which represent the largest volume of data ingested into the numerical
117 weather prediction system (Rienecker et al. 2008), necessitate subsetting the data through a thin-
118 ning routine prior to assimilation. The sub-selection of channels affects the vertical data density
119 and is not the goal of this article: in the experiments described here we have assimilated 117 chan-
120 nels, a choice very similar to NCEP at that time and the Modern-Era Reanalysis for Research and
121 Applications, Version 2 (MERRA-2, Gelaro et al. 2017), with the actual channel selection shown
122 by McCarty et al. (2016). The thinning strategy, which is the focus of this article, affects the
123 *horizontal* data density, is prescribed to a thinning mesh for each instrument type and is designed
124 to give preferences to observations likely to pass quality control (Rienecker et al. 2008).

125 AIRS clear-sky radiance data are thinned in observation space and the thinning strategy is in-
126 dependent of information from the forecast model. For the reference experiment described in
127 this study, and used in routine operations at the NASA Global Modeling and Assimilation Office
128 (GMAO) from August 2014 to May 2015, thinning is performed on a uniformly-spaced grid of
129 $145\text{ km} \times 145\text{ km}$. Within this grid, multiple instrument fields of view are present from which suit-
130 able data are chosen to be passed to the quality control routines. This selection is performed by
131 assigning a score to each radiance that is produced from a weighted combination of individual

132 scores from various suitability tests. The scoring system is designed to prefer data that minimize
133 distance from the center of the grid box and temporal departures from the analysis time, are cloud-
134 free, and are present over water. The cloud-free criterion is evaluated using a window channel as
135 a reference, with a higher score assigned to warmer brightness temperatures, indicating that the
136 signal is more likely to reach the surface rather than detecting a cloud layer. Evaluation of AIRS
137 radiance data includes additional scoring to reduce contamination from thin cirrus.

138 After thinning, the selected radiance data are evaluated for quality control by the GSI using
139 comparisons to estimates from the forecast model and nearby observations for detection of poor
140 quality data and systemic biases that may necessitate correction before assimilation (Derber and
141 Wu 1998; Rienecker et al. 2008). Quality control procedures may reject a given radiance due
142 to the presence of clouds or precipitation, uncertainty in the surface emissivity estimate, or the
143 elimination of outliers produced by gross error check. Biases may result from errors in the satellite
144 instrument, the radiative transfer model, or the background atmospheric state produced by the
145 forecast model.

146 *c. The potential of cloud-cleared radiances*

147 The use of AIRS (and other infrared instruments) has been generally restricted to the assimila-
148 tion of clear-sky radiances, which considers only channels insensitive to clouds, either within a
149 clear field of view (FOV) or with a sensitivity limited to above the cloud top. The obvious limita-
150 tions stemming from the use of clear-sky data were discussed extensively, among several others, by
151 Reale et al. (2008), Reale et al. (2009a, b), and Reale et al. (2012). In these works, the assimilation
152 of AIRS retrievals obtained under partly cloudy conditions, also known as cloud-cleared retrievals
153 (e.g., Susskind et al. 2006) was compared to the assimilation of clear-sky radiances, which was
154 and continues to be the dominant operational approach worldwide. Results showed that assimila-

tion of cloud-cleared retrievals improved: a) mid-latitude weather systems (Reale et al. 2008) via improvement of the lower tropospheric temperature structure in polar regions, probably because of a better representation of low-level stratus clouds, b) tropical cyclogenetic processes in the Atlantic (Reale et al. 2009a), c) tropical cyclones in the North Indian Ocean (Reale et al. 2009b), d) tropical cyclone-produced precipitation worldwide (Zhou et al. 2010) and e) large-scale flood-producing precipitation (Reale et al. 2012), with focus on the forecast of a major flood-producing precipitation event that occurred in Pakistan in 2010. The beneficial changes in the tropical regions were attributed to the assimilation of upper-tropospheric temperature information in areas meteorologically very active, particularly around TCs or large convective systems, in which clouds are present. For example, the assimilation of AIRS-derived information in cloudy regions could create a small upper-tropospheric temperature contrast between the area affected by a TC circulation (becoming warmer as a consequence of ingestion of AIRS data) and the surrounding environment (becoming slightly cooler), which resulted into a deeper and more confined center pressure. It was therein also argued that clear-sky radiances predominantly come from relatively stagnant regions of the atmosphere, such as large anticyclones, and are likely to exert less impact than data from cloudy regions which are generally more active.

The aforementioned results obtained by assimilation of retrievals in partially cloudy regions, while informative, have limited practical value for the forecasting community because of the almost exclusive operational use of direct radiance assimilation instead of retrievals. This choice stems partly from theoretical reasons such as, for example, avoidance of additional sources of background errors (e.g., McCarty et al. 2009). While the cloud-clearing algorithm used in AIRS version 5 retrievals did not require any model background (e.g., Chahine et al. 2006; Le Marshall et al. 2006; Susskind et al. 2006; 2011), additional practical and crucial constraints of real-time forecasting such as latency, makes the use of retrievals impractical for the operational community.

179 However, the lessons learned from the comparison between cloud-cleared retrievals and clear-sky
180 radiances cannot be ignored. Consistently better results were obtained by assimilating version 5
181 retrievals, measured with a diverse set of metrics, ranging from global skill to TC intensity and
182 extreme precipitation forecast. This is suggestive that improved coverage over meteorologically
183 active regions, which are generally affected by clouds, is an extremely important aspect. How-
184 ever, in spite of the fact that AIRS cloud-cleared radiances based on the methods of Chahine et
185 al. (2006) have been available for a long time at the NASA Distributed Active Archive Center
186 (DAAC), and that other centers have produced similar data sets, very few documented efforts of
187 assimilating AIRS radiances in cloudy regions exist in the literature (e.g., Pangaud et al. 2009;
188 Singh et al. 2011; Wang et al. 2015).

189 The purpose of this article is twofold. Firstly, it intends to provide some evidence on the benefits
190 which could be brought to operational forecasting by revisiting the overall thinning strategy with
191 a very simple adaptive approach, based on the conceptual understanding provided by the pioneer-
192 ing work by Liu and Rabier (2002, 2003), the comprehensive reviews offered, among others, by
193 Lazarus et al. (2012), and in agreement with the goals sought by operational centers (e.g., Zhu et
194 al. 2015). The second goal of this article is to show the value of AIRS cloud-cleared radiances,
195 which are not currently used in operational centers, but that could seamlessly replace clear-sky
196 radiances. In this regard, the article intends to reconcile the apparently contrasting concerns of op-
197 erational forecasts, constrained by the problems of error correlation and computational cost, and
198 the goals of the AIRS Science Team, which would advocate an improved use of AIRS products.

199 The article is organized as follows: Section 2 discusses the model and data sets, Section 3
200 provides a general description of the clear-sky experiments, with Section 4 showing the results.
201 Section 5 investigates the fraction of beneficial observations globally and on the tropical cyclone
202 scale with with the adjoint of the forecast system, Section 6 provides a general description of the

cloud-cleared experiments, with Section 7 illustrating the corresponding results. Section 8 puts the results into the context of current research, and lastly, Section 9 states the conclusions of this work.

2. Model and Data Assimilation System

All the experiments produced as part of this work were carried out with the NASA Global Earth Observing System (GEOS) data assimilation and forecast system, version 5, which merges the cubed-sphere (Lin 2004) hydrostatic version of the model (Molod et al. 2012), with the Gridded Statistical Interpolation (GSI) analysis scheme developed by the National Centers for Environmental Prediction (NCEP) and modified by the GMAO (Rienecker et al. 2008). Specifically, the version of GEOS used in this study is a frozen version (5.13.0p1) of the system, more recent than the one used to produce the Modern Era Reanalysis for Research and Applications, version 2, (Gelaro et al. 2017) run with a cubed-sphere geometry of 360×360 grid cells (c360) within each of the six faces of the gnomonic cubed-sphere grid (Putman and Lin 2007) nearly uniformly distributed around the globe. This corresponds to a horizontal resolution of about $0.25^\circ \times 0.3125^\circ$ around the equator [$40,000 \text{ km} / (360 \times 4 \text{ gridcells}) \approx 25 \text{ km}$]. The vertical resolution is 72 hybrid-eta layers extending to 0.01 hPa.

This GEOS version was the last one with a three-dimensional variational (3DVar) assimilation, and was identical to the version used semi-operationally in the GMAO until May 2015, except for disabling the vortex relocator. The current GEOS includes a hybrid four-dimensional ensemble-variational (4DEnVar) assimilation scheme, but there are several reasons for performing the experiments described in this article in a 3DVAR context. Among them, as noted by Morss et al. (2001), ingestion of data is simpler to understand and the computational cost is lower, which allows for the production of a very large number of experiments with increased statistical significance. It should

also be noted that it was essential to use the same version of the model for all the experiments, whose production spans a period of more than 2 years, starting in 2015 and ending in 2017. Finally this choice of disabling the vortex relocater was made to show how AIRS data alone can constrain the position of a storm.

3. Clear-Sky experiments setting

A first set of OSEs is performed to investigate the impact of adaptive thinning on clear-sky radiances. While the focus of this article is on cloud-cleared radiances, the findings obtained by the investigation of clear-sky radiances are a necessary prerequisite. This set consists of a number of parallel data assimilation runs starting from September 1st, 2014 and ending on November 10th, 2014, each assimilating all the observations used operationally at that time, and differing from one another only in the specific treatment of AIRS data. Seven-day forecasts are initialized at 0000 UTC daily from each analysis produced.

Specifically, the clear-sky OSE set comprises a reference experiment (RAD), which, in addition to data used operationally, assimilates clear-sky radiances thinned through a $145\text{ km} \times 145\text{ km}$ grid, which is identical to NCEP and also by the semi-operational version used by the GMAO at that time (the current GMAO system has increased the size to 180 km). This is regarded as the control experiment. Then two extreme perturbation experiments are performed, identical to RAD except for altering the AIRS global data density through much more (or less) aggressive thinning. These extreme thinning perturbations represent ‘bounding’ experiments with a drastically larger or smaller data density: a thinning box of 75 km or 300 km is used in the experiments named RAD2 and RAD3, respectively. Since only one radiance is chosen to be assimilated within the box, increasing or decreasing the thinning box size allows less or more data in the analysis.

248 More precisely, RAD2 ingests approximately four times more data than RAD, and RAD3 about
249 one quarter as many.

250 Aside from the bounding experiments, a simple, adaptive, TC-centered thinning scheme, which
251 combines two different AIRS data densities, is applied to the other experiments. Specifically,
252 the SThin experiment uses *two* different data densities resulting from thinning boxes: one inside
253 a ‘domain’ activated by the National Hurricane Center (NHC) - Joint Typhoon Warning Center
254 (JTWC) TC Best Track Data (NHC/JTWC BTD) information (also known as HURDAT2), and
255 surrounding any TC present at a given time, the other global, outside the TC domain. Specifically,
256 the data distribution in the experiment SThin uses a thinning box of 75 km (as RAD2) in moving
257 domains spanning $15^\circ \times 15^\circ$ each centered on any TC present worldwide, and a second based on a
258 thinning box of 300 km (as RAD3) used everywhere else. This results in a global density of about
259 one quarter compared to the control, except around TCs, where the density is four times larger
260 than RAD. In short, SThin has the same density as RAD2 inside the TC domains, and the same as
261 RAD3 outside the TC domains. Whenever there is a TC somewhere on the globe, the NHC/JTWC
262 BTD information (which contains, among other data, the TC position) is used to create a domain
263 around the TC in which denser AIRS data coverage is assimilated. During the period in which
264 the experiments take place, there are 23 TCs worldwide, and at least one TC for about 90% of
265 the duration of the assimilation. More precisely, the adaptive thinning is used 266 times over 284
266 6-hourly time steps, and up to 5 TCs are present simultaneously (17 Sep 2014) on all basins.

267 In a real-time set up, the BTD information could be seamlessly replaced with the ‘TC vital’
268 information (Trahan and Sparling 2012). The data densities in the experiments are listed in Table 1
269 and can be visualized in Fig. 1, which magnifies a region over the western North Atlantic, around
270 Hurricane Gonzalo at 0600 UTC 15 October 2014, for clarity. It is important to note that the size of
271 the TC domain ($15^\circ \times 15^\circ$) in the experiment SThin results from being the best of a number of five

272 experiments. The remaining four are not discussed in this paper, but just listed for completeness
273 sake, and shortly commented. These are named SThin2, SThin3, SThin4, and SThin5. The first
274 two alter the thinning box sizes, the second two the TC domains. Finally, the experiment named
275 OPS represents the version of the model that was used operationally by the GMAO at the time,
276 and as late as 2015. OPS is exactly the same model version as RAD, and differs only because
277 the vortex relocator is used in the former. There is also another very minor difference in the
278 experiment setup: the sea surface temperatures (SSTs) used in the assimilation are updated daily
279 at 0000 UTC in RAD, and at 1200 UTC in OPS, but this cannot possibly affect skill. While we
280 refer to RAD as the rigorous control experiment, the additional reference to OPS is very important
281 because it shows that the use of the vortex relocator, thought to be useful for TC purposes, is
282 slightly harmful to the global skill. Moreover, this article will suggest in the following sections
283 that the supposed improvement to the TC analysis caused by the vortex relocator could be obtained
284 instead by adaptive assimilation of AIRS cloud-cleared data.

285 Fig. 1 illustrates the limitations of the clear-sky approach, in which only channels thought com-
286 pletely unaffected by clouds are evaluated for the thinning and then assimilated. In fact, at the
287 RAD data density level, a large data void area can be seen around hurricane Gonzalo, because
288 all the channels considered ‘cloud-contaminated’ are rejected before the thinning. However the
289 RAD2 data distribution, even if still based upon clear-sky radiances, provides some hint of the
290 hurricane outer structure, because of the use of approximately four times more radiances. In fact,
291 particularly evident are some banded structures to the north and east of the center. A smaller
292 thinning box means that some observations can be accepted by the cloud-detection algorithm in
293 narrow clear filaments between rain bands. The smaller the box, the higher the likelihood that
294 some radiances in small clear areas can be assimilated. The experiment RAD3 uses a 300 km thin-
295 ning box, which causes AIRS data to be reduced to approximately one quarter compared to RAD.

In contrast with RAD2, the RAD3 data distribution gives almost no information in the proximity of the hurricane's center.

4. Clear-sky experiment results

Figure 2 shows the 500 hPa global anomaly correlation for all the experiments whose coverage is shown in Fig 1, as a function of forecast time. The differences of each experiment with respect to both OPS and RAD are also displayed in the same figure. When the OPS experiment serves as the reference for this plot, the improvements or degradations in skill shown in the center panel are plotted with respect to the OPS forecast. Similarly, the figure below allows to discern improvements or degradations compared to RAD. It is worth comparing against both: in fact, while RAD is the 'rigorous' control experiment, OPS represents the model that was used operationally at that time, and one goal of this article is to show that, aside to the large improvements in TC representation (to be shown later), no degradation of global skill occurs as a consequence of the adaptive thinning.

The most striking result evident from Fig. 2 is that the two bounding experiments, RAD2 and RAD3, characterized by the most extreme thinning, produce the worst and best global skill of all the experiments, respectively. The improvement in skill for RAD3 is statistically significant compared to OPS. RAD is significantly better than OPS, indicating that the use of the vortex relocator alone, while profitable from a TC forecasting perspective, may be slightly harmful to the global skill, (since it is reasonable to assume that no impact comes from updating SSTs at 0000 UTC or 1200 UTC, which is, as stated, the only other difference between RAD and OPS). As previously noted, the SThin is chosen as the best among a number of adaptive thinning configurations listed in Table 1. It is worth nothing that all have more global skill than the operational GEOS of that time, but slightly less than SThin (not shown).

319 The response to the two bounding experiments is also captured by other metrics. For example,
320 Fig. 3 shows the root-mean-square-error (RMSE) computed over the tropics for temperature in the
321 24-h and 120-h forecasts. RAD3 produces a small improvement and RAD2 a large deterioration
322 compared to RAD and OPS in the 24-hour. The effect is maintained, even if smaller, up to day 5.

323 It is possible that the surprising beneficial effect of more aggressive data thinning for clear-sky
324 AIRS radiances can be explained in terms of error correlation. Following LR03, it would seem
325 that error correlation, for the AIRS radiances on the scales in which they are operationally used,
326 exceeds a threshold so that the additional observations are harmful.

327 However, the situation changes drastically when observing active, rapidly evolving features with
328 tight gradients. The chosen example is Hurricane Gonzalo. Gonzalo was a TC that formed and
329 developed over the west Atlantic between 12 and 19 October 2014 (Brown 2015). It formed east
330 of the Leeward Islands, started recurving northwestward while undergoing rapid intensification.
331 It reached its peak intensity on the 16th, becoming a category 4 storm with a center pressure of
332 940 hPa. After landfall over Bermuda, the hurricane accelerated northward and then very rapidly
333 northeastward, while still retaining hurricane strength and a tropical structure as far north as $45^{\circ}N$.
334 Extratropical transition (ET) began at about $50^{\circ}N$ with Gonzalo's remnants becoming a very in-
335 tense mid latitude cyclone which produced, according to the United Kingdom Meteorological
336 Office, very strong winds on the British Isles (¹). Gonzalo is a good case for this research because
337 its track was intercepted by several passes of the Aqua satellite, thus guaranteeing almost optimal
338 AIRS coverage, which facilitates the investigation of the impacts due to changes in AIRS data and
339 thinning strategy.

340 Fig 4 shows the zonal vertical cross-section, and horizontal transects at 850 hPa, across the center
341 of Hurricane Gonzalo, in the RAD, RAD3 and SThin analyses, at 1200 UTC 16 October 2014,

¹<https://blog.metoffice.gov.uk/2014/10/21/top-uk-wind-speeds-as-gonzalos-remnants-felt/>

the time of its maximum intensity. The RAD cross-section shows a reasonable representation of the storm, but affected by an excessive asymmetry not supported by observations, and much weaker than observed, since winds of above 60 m s^{-1} at 700 hPa were reported (Brown 2015). The RAD3 analysis shows the impact of reducing the AIRS data density over the storm: while the RAD3 global skill increased substantially, the relative absence of AIRS information over the storm (recall Figs. 1 and 2), leads to a deterioration of the TC structure compared to RAD. Intensity is drastically reduced, and the asymmetry is further increased. However, the TC structure resulting from the SThin adaptive thinning is substantially better, with a tighter eye, a stronger warm core, and a more symmetric structure. Since the SThin global skill is virtually indistinguishable from RAD3 (Fig. 2), and the TC structure appears improved, the adaptive strategy of combining the global aggressive AIRS thinning of RAD3 with the denser data coverage around Gonzalo appears to be a good compromise.

These findings are consistent with those for other TCs present during the experiment period (not shown) and can be interpreted, following LR03, as evidence of a scale-dependent error correlation affecting the assimilation of AIRS radiances.

In fact, these OSEs are an indication that infrared data from hyperspectral instruments could be thinned much more aggressively, because error correlation could be present on a global scale at the current thinning level (as used in OPS or RAD), and that the consequent volume of AIRS radiances assimilated globally is excessive. RAD3 consistently performs better than RAD, hence the intuitive response to simply increase the size of the thinning box to assimilate a lower density of radiances. However, since the analyzed structure of TCs appears to benefit by additional AIRS data on the TC scale, it is likely that error correlation is much lower over the spatial and temporal scales affected by TCs. RAD2, in spite of having a much lower skill globally, improves the TC analysis compared to RAD (not shown), while RAD3 acts in the opposite way: it increases the global

skill but degrades the analyzed TC structure. SThin, which combines RAD2 and RAD3 densities, suggests a scale dependence for error correlation, in agreement with the conceptual understanding offered by LR03, and indicates a TC-centered adaptive thinning as a possible pathway.

The reason why SThin global skill is close, but not superior, to RAD3, may be also interpreted in light of the understanding provided by LR03, concerning an error correlation threshold beyond which additional observations are harmful. In the experiments herein described the threshold is not known: the fixed size of the TC domain, that does not take into account TC scale or the particular stage in the TC life cycle, may include denser data coverage at times and locations in which additional data are harmful. While the SThin configuration was selected as the best among those examined (recall Table 1), it is undoubtedly suboptimal, because it cannot rigorously separate observations that are beneficial from the ones that are not. A more refined approach could involve variable TC domain sizes, based on the TC scale (which is available from the 'TC vital' information).

5. Use of the adjoint of the forecast model

The evidence provided so far by the first set of OSEs is indicative that with the current thinning strategy for AIRS clear-sky radiances, correlated observation errors may be negatively impacting the large scales. However, these correlations do not appear to have negative impact on the scale of tropical cyclones. This suggests that a simple strategy, focused on assimilating fewer AIRS radiances globally, except around TCs, could be successful.

Additional evidence can be provided with the use of a different methodology to assess observational impacts: the adjoint-based forecast sensitivity observation impact (FSOI) technique, first proposed by Langland and Baker (2004). Benefits arising out of OSEs and adjoint models have been studied and extensively compared, for example in the context of The Observing system Re-

389 search and Predictability EXperiment (THORPEX, created in 2003 by the World Meteorological
390 Organization as a testbed to compare advances and theoretical understanding in data assimilation
391 and observing strategies), by Rabier et al. (2008). Specifically, it is clarified that observing system
392 experiments (OSEs) and techniques based on the adjoint of the forecast model are complemen-
393 tary methodologies to assess contributions of different observing systems. Gelaro and Zhu (2009)
394 discuss in detail the usefulness and potential of OSEs and adjoint models. Gelaro et al. (2010)
395 compare the impact of assimilated observations on short-range forecast errors in 3 different fore-
396 cast systems using an adjoint-based FSOI.

397 The construction of the GMAO adjoint-based FSOI system follows Langland and Baker (2004)
398 and Trémolet (2008). Two forecasts are integrated 24 hours beyond the analysis time of interest,
399 one initialized from the analysis state itself and one from the background state. The reduction
400 in forecast error from the background to the analysis forecast results only from the observations
401 assimilated at analysis time. A response function provides a scalar measure of the forecast error
402 by applying a moist energy norm. The gradient of this function with respect to the model variables
403 is integrated backwards to the analysis time 24 hours prior using the adjoint of the model. The
404 output from the adjoint describes the regions that are most sensitive to the growth of the forecast
405 errors (in a tangent linear sense) at the initial time. In effect, changes in these locations would
406 have a larger impact on the size of the forecast errors than changes elsewhere, and observations in
407 these locations have the largest impact. Translation of this model sensitivity onto each observation
408 is achieved with an integration of the adjoint of the data assimilations system (Trémolet 2008;
409 Gelaro et al. 2010).

410 The combined use of adjoints and OSEs represents a powerful tool, because the adjoint based
411 FSOI can be used to analyze the effects on all the observations of different thinning box sizes
412 applied to AIRS. The adjoint of GEOS benefits from a full suite of moist physics schemes (Hold-

away et al. 2014; Holdaway et al. 2015) allowing for proper interpretation of observation impact where moist processes are important.

Two FSOI configurations, global and Gonzalo-centric, are considered in order to assess the overall impact of AIRS observations. In the global configuration, the adjoint is initialized for the entire global domain and the impacts are also measured globally. In the Gonzalo-centric configuration, the adjoint is initialized for a limited domain which encompasses the entire life cycle and track of Hurricane Gonzalo. For this configuration, the impact is assessed only within another domain around the initialization domain. This is done to prevent including spurious impact from remote observations, which can occur due to sensitivity to gravity wave structure and through observation weighting, and is important for constructing informative normalized metrics. Globally, the FSOIs are computed at 0000 UTC. For the Gonzalo-centric domain, the FSOIs are computed at 0600 UTC and 1800 UTC, consistent with the timing of AIRS overpasses. Figure 5 shows the track and intensity of Hurricane Gonzalo with the two domains encompassing the storm. The inner domain (spanning from $75^{\circ}W$ to $35^{\circ}W$ and from $10^{\circ}N$ to $40^{\circ}N$) shows the response function domain, the outer domain (spanning $115^{\circ}W$ to $5^{\circ}E$ and from $30^{\circ}S$ to $85^{\circ}N$) is the region in which the impact is assessed. The outer domain is chosen so that 95% of the total observation impact is retained.

Fig 6 shows the fraction of beneficial observations resulting from the RAD, RAD2, and RAD3 experiments, computed using the global FSOI configuration. Here, the term ‘beneficial’ refers to observations that reduce the 24-hour global error, as measured by the response function. The fraction of beneficial AIRS observations slightly decreases in RAD2 and increases in RAD3. This, together with the changes in global skill seen in Fig 2, suggests that error correlation is *reduced* by decreasing the AIRS data density, in agreement with LR03. However, the fact that CrIS data also respond in the same way to the increase and decrease of AIRS data density, even if CrIS data density is *not modified* in these experiments, is remarkable and strongly suggestive that cross-

instrument error interactions should be considered. This is reasonable because of the similar orbits, but is beyond the purpose of this article and will be addressed by a study in preparation. However, for the purpose of this article, it is most important to verify if the fraction of beneficial observations changes when affected by rapidly evolving meteorological features.

To this purpose, the same impacts seen in Fig 6 are recomputed but with the response function calculated over a smaller spatial and temporal domain. Figure 7 shows the fraction of beneficial observations between 0600 UTC 12 October and 1800 UTC 19 October, computed using the Gonzalo-centric FSOI configuration. The response function that initializes the adjoint spans from $75^{\circ}W$ to $35^{\circ}W$ and from $10^{\circ}N$ to $40^{\circ}N$; fractions are computed for a domain spanning from $115^{\circ}W$ to $5^{\circ}E$ and from $30^{\circ}S$ to $85^{\circ}N$. The figure shows the average across all 0600 UTC and 1800 UTC analyses, the approximate time Aqua passes over the domain, from 12 October 2014 to 19 October 2014. The most striking result is the increase of AIRS radiances impact in the RAD2 case, indicating that a much denser data distribution is beneficial over the spatial and temporal scale that is affected by the Hurricane Gonzalo. It is worth noting that the adjoint forecast are computed twice, at the times in which the area over which Gonzalo is active is affected by direct AIRS passes, which increases the confidence in the result. Moreover, the environment that controls Gonzalo's large-scale low-level moist flow largely exceeds the scale of the domain in which the observation impacts are evaluated. Specifically, the easterly flow entering the domain from the East and associated with the African Easterly Jet is a very sensitive feature characterized by strong meridional temperature gradients, where the detailed infrared information provided by additional AIRS data can provide a beneficial impact on the analysis, as shown in previous studies (e.g., Reale et al. 2009a).

It is important to note the difference between Figs. 6 and 7 in combination with the results discussed about Figs. 2 and 4: denser coverage in RAD2 decreases forecast skill and AIRS impacts

461 in global metrics, but it can increase forecast skill and AIRS impacts for Gonzalo. Conversely,
462 the sparser data coverage of RAD3 results in an increase in skill and AIRS impact globally but
463 decrease for Gonzalo. These results in unison are strongly suggestive that error correlation acts on
464 a smaller scale in areas affected by hurricanes, and that a TC-centered adaptive approach may be
465 beneficial.

466 **6. Cloud-Cleared experiments setting**

467 Table 2 and Figure 8 describe the configuration of the experiments assimilating cloud-cleared ra-
468 diances, and illustrate their corresponding data density. The experiment named CLD differs from
469 RAD only because cloud-cleared radiances are assimilated instead of clear-sky. The global data
470 density, consequent to a thinning box choice of 145 km , is about the same. However, the specific
471 *distribution* of the data is not the same, as can be noted by comparing Figs 8 and 1. Clear-sky and
472 cloud-cleared radiances are completely different products, and as such cannot be expected to cor-
473 respond precisely. As discussed by Reale et al. (2012), which focused on retrievals, the underlying
474 cloud-clearing algorithm uses a different channel selection than clear-sky, and the cloud-cleared
475 radiances are extracted from an array of 3×3 FOVs, so an exact correspondence of data location
476 cannot be expected even if the thinning box is the same. Aside from the precise location of in-
477 dividual assimilated observations, it should be noted that the mere position of CLD observation
478 minus forecast (O-F)s reveals slightly more meteorological structure around the center of Gonzalo
479 than RAD does. This stems from the ability of the cloud-clearing algorithm to extract data from
480 areas that are affected by partial cloud coverage. As for the clear-sky case, two extreme ‘bound-
481 ing’ experiments, named CLD2 and CLD3, are performed. The CLD2 data distribution seen in
482 Fig 8 results from a thinning box of 75 km which produces about 4 times more data than CLD,
483 whereas CLD3 data distribution is obtained by thinning cloud-cleared radiances with a thinning

box of 300 km which retains about one quarter of the CLD data. Two adaptive thinning selections of cloud-cleared data are discussed in this work: SThin_CLD, combining the data density of CLD3 globally and the data density of CLD2 inside a moving domain of $15^\circ \times 15^\circ$ centered around any TC in the globe, and activated by the BTD information, and SThin2_CLD, which combines CLD density inside the TC domain and CLD3 globally.

7. Cloud-Cleared experiments results

a. Impact on global skill

Figure 9 shows the anomaly correlation of all the cloud-cleared experiments compared to OPS and RAD, which are both used as the reference. As for the clear-sky experiments, the bounding experiments CLD2 and CLD3 produce the highest and lowest skill, respectively, but the drop of skill in the CLD2 case is much more dramatic than in RAD2 (recall Fig. 2), indicating that an excessively dense coverage in cloudy radiances is even more harmful. However, the two adaptive thinning experiments, both with a global data density of about one quarter that of CLD, are clustered together without significant difference in skill from RAD. Moreover, none of them is worse than OPS, which was the operational GEOS version at the time, identical to RAD except for the use of the vortex relocator. The temperature RMSE as a function of height over the tropics, computed for CLD, CLD2, and CLD3 against RAD, for the 24 h and 120 h forecasts shows a consistent pattern (and a behavior similar to the one noted in Fig 3 for the bounding clear-sky experiments): CLD3 very slightly outperforms RAD while CLD2 causes a large increase in error (not shown).

This suggests that errors of cloud-cleared radiances are much more correlated than those of clear-sky radiances. Following Daley (1993) the observation error can be separated into an in-

506 strummental error and a representativeness error. It is possible that the representativeness error of
507 the cloud-cleared radiances is smaller and as such the errors are more correlated if assimilated at
508 the same density as the clear-sky radiances. Whatever the cause, the important fact is that cloud-
509 cleared radiances, if assimilated with a data density of about one quarter the one of the currently
510 assimilated clear-sky radiances, can produce a comparable, or even slightly higher, global skill in
511 the GEOS.

512 *b. Impact on tropical cyclone analysis*

513 Since the purpose of this work is to improve the analyzed representation of tropical cyclones by
514 making a better use of AIRS, three TCs that occur during the period are investigated: Edouard and
515 Gonzalo in the Atlantic, and Vance in the Eastern Pacific. Of these, Gonzalo is the most favorable
516 from an AIRS coverage perspective. However, cloud-cleared radiances provide a positive impact
517 on all three.

518 Edouard can be considered as a slowly developing Cape Verde system since its origins can be
519 traced to an African Easterly Wave that exited the coast of western Africa on September 6th, with
520 closed circulation sufficiently defined to be a tropical depression only five days later, on 1200
521 UTC 11 September 2014 (Stewart 2014) at about $35^{\circ}W$. Edouard underwent rapid intensification
522 becoming a category 3 hurricane and reaching peak intensity on the 16th and 17th, and then rapidly
523 weakening on the 18th, while turning eastward, embedded in the westerly flow. From the point of
524 view of this research, it represents a less than optimal case, because the storm quickly deepens and
525 quickly dissipates, not benefiting from the information that several Aqua passes over the mature
526 storm would have provided. In spite of the coverage limitation, the use of AIRS cloud-cleared
527 radiances positively affects the representation of the storm.

528 In fact, Fig 10 illustrates the analyzed representation of center pressure for Edouard in 3 experi-
529 ments (RAD, CLD3, and SThin2_CLD), compared to the observed Best Track data. Results from
530 SThin_CLD are not shown for clarity, being consistently between RAD and SThin2_CLD, also
531 for other cases. In other words, SThin2_CLD provides the best representation of TCs through-
532 out the experiment period on all basins. Both analyses that assimilate cloud-cleared data produce
533 a representation of the storm closer to the observations, with slightly deeper values than RAD.
534 However, the zonal vertical cross section of Edouard taken at the time of its second intensity
535 peak (1800 UTC 17 Sep) shows more clearly (Fig 11) that horizontal and vertical structure of the
536 storm is positively affected by the assimilation of cloud cleared data and that the adaptive thinning
537 methodology brings the largest intensification. Note for example the circulation becoming closed
538 on the northwest quadrant in the SThin2_CLD experiment, and the corresponding increase in ver-
539 tical extent of the thermal anomaly. While the actual strength of Edouard is still underestimated,
540 the SThin2_CLD experiment shows an intensification of about 10 m s^{-1} compared to RAD.

541 Gonzalo's analyzed center pressure is shown in Fig 12. The improvement brought by adaptively
542 thinned cloud-cleared radiances is much more dramatic, reaching maximum intensity at 1800 UTC
543 16 October, just six hour after peak intensity, (when the observed center pressure was still very
544 low, at 942 hPa), and with 20 hPa deeper compared to RAD. Gonzalo represents an almost ideal
545 situation for the adaptive thinning strategy, because it is a sufficiently long-living storm (and hence
546 is covered by multiple Aqua passes), it does not undergo dramatic scale changes, and it is neither
547 too small (which would pose resolution problems) or too large (with a circulation exceeding the
548 swath of the AIRS passes).

549 The importance of good AIRS coverage is particularly evident in Fig. 13, which shows the zonal
550 vertical cross-sections across Gonzalo, and the corresponding horizontal sections at 850 hPa, in
551 the RAD, CLD3 and SThin2_CLD cases at 1800 UTC 16 October 2014, very close to its peak

intensity. The assimilation of cloud-cleared radiances at a CLD3 density level does not exert an impact on Gonzalo's structure compared to RAD, but the denser coverage of SThin2_CLD provides a dramatic speed increase of more than 15 m s^{-1} , with peak speed of about 45 m s^{-1} at about 700 hPa which, is the level where the maximum speed of 68 m s^{-1} was measured by an US Air Force Hurricane Hunter aircraft at 0000 UTC 17 October (Brown 2015).

Vance was a small-scale, relatively short-lived Hurricane, which lingered between October 30th and November 2nd at tropical depression intensity level, underwent a rapid intensification on November 2nd, reached category 2 and peak intensity on November 3rd, and very rapidly dissipated on November 4th. This represents a very difficult case for a global DAS, because of intrinsic problems associated with poor data coverage and resolution. Figure 14 shows the analyzed minimum center pressure as a function of time, and confirms that the storm was almost not seen by the DAS in the RAD case. The center pressure never reaches 1000 hPa and does not show any hint of intensification. The cloud-cleared cases are slightly better, both going below 1000 hPa, although strongly underestimating its depth. However, the impact of cloud-cleared radiances on the storm structure is not negligible (Fig. 15). While the RAD vertical section and circulation reveal an open wind structure, with a shallow warm core not reaching the mid troposphere, the CLD3 case shows a better defined velocity vertical structure, a more pronounced warm core reaching 300 hPa, and a well defined low-level circulation. Interestingly, the SThin2_CLD experiment, while better than RAD, does not outperform CLD3. The AIRS coverage (not shown) is relatively poor for this short-living storm: there are no Aqua passes over Vance at its peak intensity, suggesting that CLD3, which probably produces a slightly better representation of the global scale (recall the better CLD3 global skill in Fig.9), influences the representation of Vance more than SThin2_CLD since no additional AIRS data are assimilated in spite of the adaptive strategy.

576 The assimilation of adaptively thinned cloud-cleared AIRS radiances does not have a signif-
577 icant impact on error track statistics during the chosen period, as for the case of clear-sky ra-
578 diances. Compared to RAD, track errors produced by most configurations differ little. For ex-
579 ample, SThin_CLD track error at day 3 for Gonzalo is about 20 km smaller than RAD, whereas
580 SThin2_CLD produces a 72-hour track error 30 km larger than RAD. As a reference, the RAD
581 error was about 290 km, slightly larger than the corresponding errors of 250 km by the NCEP
582 GFS and 265 km of the ECMWF model (Brown 2015). The impact of the adaptive strategies on
583 forecast track error for the other storms investigated in these experiments is also negligible (not
584 shown).

585 However, the impact is significant in intensity forecast, up to 48 hours. This is reasonable
586 because of the improved analyzed TC structure. In particular, the type of impact appears to be
587 different for storms that have a good AIRS coverage during their life cycle and storm that do not.
588 Figure 16 showcases two representative cases, Gonzalo and Vance, showing the RMS error for the
589 predicted center pressures of the two storms as a function of forecasting time. For Gonzalo, there
590 is a significant improvement in the SThin2_CLD case, which is consistent with the substantially
591 improved analysis seen in Figs. 12 and 13. The impact on intensity forecast in the CLD3 is, on the
592 contrary, negligible.

593 In the case of Vance, the situation is different, with CLD3 giving the best forecast and
594 SThin2_CLD providing a smaller improvement compared to RAD. This is consistent with the
595 fact that Vance is small scale, not well resolved at the GEOS resolution, and that the time of
596 full intensity is short and not covered by a full AIRS pass. As such, the additional information
597 provided by the adaptive thinning is not used. However, the information provided by the cloud-

598 cleared radiances on the large scale, brings some improvement in both cases, consistent with the
599 slightly improved analysis seen in Figs. 14 and 15. It is interesting to observe that the impact on
600 intensity forecast decreases as a function of forecasting time in Gonzalo’s case, and increases in
601 Vance’s case. This can be explained considering that the improvement is brought by the addi-
602 tional information on the TC structure provided by adaptive thinning in Gonzalo’s case, and by
603 the improvement brought on the large scale, which is likely the beneficial factor in Vance’s case.

604 This contrasting behavior, while confirming that cloud-cleared radiances are beneficial in both
605 cases, suggests that a more refined adaptive strategy should include a scale-dependence for the
606 size of the TC domain in which denser coverage is to be used instead of a fixed TC-domain as
607 done in these experiments. Moreover, the limitations caused by insufficient AIRS coverage for
608 short-lived storms could be a consequence of the 3DVAR assimilation, and may be mitigated by a
609 four dimensional assimilation. However, it is important to clarify that the cloud-cleared adaptive
610 approach has never produced a negative impact on any of the TCs present during this period over
611 all basins: the impact is strongly positive when coverage is good, or neutral when coverage is not
612 optimal (not shown).

613 Finally, the adjoint of the forecast and analysis models are used in the same way as in the clear-
614 sky case, with focus on the cloud-cleared experiments CLD3 and CLD, and the adaptive thinning
615 SThin2_CLD. The same two FSOI configurations, global and Gonzalo-centric (recall Fig 5), are
616 considered in order to assess the overall impact of AIRS cloud-cleared observations. In the global
617 configuration, the adjoint is used to assess 0000 UTC analysis times for the entire global domain
618 and the impacts are also measured globally. In the Gonzalo-centric configuration, the adjoint is
619 used to assess the 0600 UTC and 1800 UTC analysis times for a limited domain, which encom-
620 passes the entire life cycle and track of Hurricane Gonzalo. The results presented below show
621 the average observation impacts for the two analysis times. By assessing 0600 UTC and 1800

UTC analyses all times that Aqua flies over the domain are taken into consideration. Figure 17 shows the fraction of beneficial observations on the global domain, comparing the experiments CLD, CLD3 and SThin2_CLD; Figure 18 compares the fraction of beneficial observations over the Gonzalo-centric domain. On the global scale, CLD3 has the largest fraction of beneficial observations, in agreement with the best global skill seen in Fig 9. However, within the Gonzalo-centric framework, it is the SThin2_CLD configuration that contains the largest fraction of beneficial observations. This suggests that the adaptive thinning of cloud-cleared radiances is most effective, even more so than when applied to clear sky observations. This is likely due to the much higher information content in the cloud-cleared radiances. It is worth remembering, for example, that one cloud-cleared radiance is obtained from up to nine field of views within the same footprint (Chahine et al. 2006; Susskind et al. 2011).

8. Discussion

Several caveats are necessary to place this work into a proper context. First, the focus of the research is on AIRS. Ongoing work at this time has shown that the error correlation problem does not affect just AIRS, but also other hyperspectral instruments such as CrIS and IASI. Specifically, evidence is suggestive not only that the issue of excessive data density at the current thinning levels may exist for other instruments, but also that an interaction between data from different instruments is possible. As a consequence, a more robust strategy should consider revisiting the thinning for the three instruments together. While this is beyond the purpose of this work, it is important to state that the thinning levels that appear to be the best for AIRS from this work, could need further adjustments when changes in thinning for other sensors are also included.

Second, the results obtained from the adaptive thinning reveal a scale dependence and are strongly sensitive to coverage. In fact, the specific adaptive thinning schemes seem to benefit

different TCs in different domains. For example, Gonzalo is a very favorable case because several passes occur over its lifetime, and its scale does not exceed the swath of the AIRS pass. For Vance, the rapid evolution and the small scale make the adaptive configurations used here of little use. For other storms not shown in this work, such as the typhoon Vonfong, whose effects on the large-scale environment largely exceed the swath of AIRS, the response is essentially neutral to AIRS thinning changes.

Third, the limitations caused by the 3DVAR could act in two directions. From one side, it is possible that the limitations caused by coverage are reduced once observations are continuously assimilated in time. From the other, it is possible that the thinning levels suitable for a 3DVAR configuration need to be altered in a 4DVAR system.

Fourth, cloud-cleared radiances have not been studied extensively in a data assimilation context. A deeper investigation of their quality control could be beneficial to understand their different responses to thinning. It is possible that the representativeness error of cloud-cleared radiances be smaller than clear-sky radiances, since they represent both clear areas and areas that are partly affected by clouds, and result from an average of more FOVs, which reduces their signal to noise ratio. A smaller representativeness error could be one cause of larger error correlation. While this lies beyond the scope of this article, it is nevertheless an important aspect to consider in future investigations aiming at the operational use of them.

Fifth, only the horizontal error correlation problem is addressed in this work. The problem of correlation between channels (e.g. Todling et al. 2015) is not investigated. It is possible that cross-channel error correlation could be altered by the cloud-clearing procedure.

Sixth, while the impact of cloud-cleared radiances from AIRS and CrIS has been proven to be beneficial in a regional model context with focus on TCs (Wang et al. 2015; Wang et al. 2017), and the possibility of adaptive thinning could be explored, the results from this work would probably

not be directly applicable without additional research. The concept of ‘optimal data density’ could be drastically different in a regional model context. For example, Lin et al. (2017) illustrates the beneficial impact of AIRS on short range forecasts even in a data rich area, after undergoing a preprocessing that involves channel selection and bias-correction spinup.

9. Conclusions

Notwithstanding the limitations discussed in the previous section, there are two findings suggested by the two sets of OSEs and the adjoint results herein described. The first appears to be evidence that AIRS clear-sky radiance errors at the current thinning level are strongly correlated on a global scale, but that error correlation is reduced around tropical cyclones. This finding is intuitively consistent with the conceptual understanding provided by LR03.

The second finding is that there is great potential benefit in using cloud-cleared radiances, rather than clear-sky radiances, in an operational context. Their primary effect on TC representation (consistent with already known impacts of assimilating cloud-cleared retrievals e.g., Reale 2009b) is to create a very strong and concentrated temperature anomaly in the upper troposphere, (e.g., Fig. 13) with gradients of the order of more than $10^{\circ}C/100km$ which translates, through hydrostatic adjustment, to a lower central pressure. The thermal anomaly is present for all TCs worldwide (not shown) and has the combined effect of deepening the storms and also adjusting their positions. In fact, the peak of the temperature anomaly that is induced by the assimilation of cloud-cleared radiances is aligned with the storm center. Consequently, the use of cloud-cleared radiances negates the need of a vortex relocator, which has been noted in this paper to reduce global skill (recall comparison of OPS with RAD in Figs. 2 and 9) and has a computational cost. Cloud-cleared radiances are distributed from the Goddard DAAC and are available in real time.² Alternatively,

²https://daac.gsfc.nasa.gov/datasets/AIRI2CCF_V006/summary?keywords=AIRS%20cloud%20cleared%20radiances

691 operational centers could produce their own cloud-cleared radiances by developing an algorithm
692 or modifying existing ones (e.g., Susskind et al. 2014), which could improve latency. The errors of
693 cloud-cleared radiances appear to have higher spatial error correlations than clear-sky radiances,
694 meaning they can and should be thinned more aggressively. A density of about one-quarter of the
695 cloud-cleared radiances results in retaining the same global skill as RAD, while substantially im-
696 proving the TC analysis. These facts should be considered in an operational environment, because
697 indicate the possibility of reduced computational costs.

698 The underlying motivation for this article was to explore the possibility of error correlation
699 affecting the forecast skill in response to the assimilation of AIRS radiances. OSEs with different
700 adaptive configurations suggest that the scales of observational error correlation for AIRS are
701 much smaller for TCs. The use of the adjoint of the forecast model is supportive of this idea
702 and encourages further research on a simple, TC-based, adaptive scheme for all hyperspectral
703 data. In addition, this work shows that cloud-cleared radiances, if used at a much sparser level
704 than clear-sky radiances globally except around tropical cyclones, can bring a comparable or even
705 slightly superior global skill, while drastically improving the TC analysis and intensity forecast in
706 the GEOS. The implications for TC operational forecast improvement are noteworthy and worth
707 exploring.

708 *Acknowledgments.* The authors gratefully acknowledge support by Dr. Ramesh H. Kakar (NASA
709 HQ) through NASA Grant NNX14AK19G and Dr. Tsengdar Lee (NASA HQ) for allocations on
710 NASA High-End Computing resources. All simulations were performed at the NASA Center for
711 Climate Studies (NCCS) in Greenbelt, Maryland. AIRS data are distributed by the NASA Dis-
712 tributed Active Archive Center (DAAC) Goddard Earth Sciences Data and Information Services
713 Center (GES DISC).

- 715 Bauer, P., A. J. Geer, P. Lopez, D. Salmond, 2010: Direct 4D-Var assimilation of all-sky radiances.
716 Part I: Implementation. *Q.J.R. Meteorol. Soc.*, **136**, 18681885. doi:10.1002/qj.659
- 717 Bishop, C. H., and Z. Toth, 1999: Ensemble transformation and adaptive observations. *J. Atmos.*
718 *Sci.*, **56**, 17481765.
- 719 Bondarenko, V., T. Ochotta, and D. Sauple, 2007: The interaction between model resolution,
720 observation resolution and observation density in data assimilation: a two-dimensional
721 study. 87th AMS Annual Meeting, January 13-18, 2007, San Antonio, Texas, [Available
722 online at https://ams.confex.com/ams/87ANNUAL/techprogram/paper_117655.htm]
- 723 Brown, D. P, National Hurricane Center. Tropical Cyclone Report. Hurricane Gonzalo
724 (AL082014), 12-19 October 2014. National Hurricane Center, 30 pp. [Available online
725 at: www.nhc.noaa.gov/data/tcr/AL082014_Gonzalo.pdf]
- 726 Chahine, M. T., and Coauthors, 2006: AIRS: Improving weather forecasting and providing new
727 data on greenhouse gases. *Bull. Amer. Meteor. Soc.*, **87**, 911926, doi:10.1175/BAMS-87-
728 7-911.
- 729 Daley, R., 1996: *Atmospheric Data Analysis*. Publisher: Cambridge Atmospheric and Space
730 Science Series, Cambridge, UK, 457 pp.
- 731 Derber, J., and W.-S., Wu 1998: The use of TOVS cloud-cleared radiances in the NCEP SSI
732 analysis system. *Mon. Wea. Rev.*, **126**, 22872299.
- 733 Gelaro, R., R. Langland, G. D. Rohaly, and T. E. Rosmond, 1999: An assessment of the singular
734 vector approach to targeted observing using the FASTEX dataset. *Quart. J. Roy. Meteor.*
735 *Soc.*, **125**, 32993328.

736 —, and Y. Zhu, 2009: Examination of observation impacts derived from observing system experi-
737 ments (OSEs) and adjoint models. *Tellus A*, **61:2**, 179-193.

738 —, R. H. Langland, S. Pellerin, and R. Todling, 2010: The THORPEX Observation Impact Inter-
739 comparison Experiment. *Mon. Wea. Rev.*, **138**, 40094025.

740 —, W. McCarty, M. J. Suarez, R. Todling, A. M. Molod, L. L. Takacs, C. Randles, A. Darmanov,
741 M. G. Bosilovich, R. H. Reichle, K. Wargan, L. Coy, R. I. Cullather, S. R. Akella, V.
742 Bachard, A. L. Conaty, A. da Silva, W. Gu, R. D. Koster, R. A. Lucchesi, D. Merkova, G.
743 S. Partyka, S. Pawson, W. M. Putman, M. M. Rienecker, S. D. Schubert, M. E. Sienkiewicz,
744 and B. Zhao, 2017. The Modern-Era Retrospective Analysis for Research and Appli-
745 cations, Version-2 (MERRA-2). *J. Climate*, **30**, 5419-5454. DOI 10.1175/JCLI-D-16-
746 0758.1.

747 Holdaway, D. R., R. M. Errico, R. Gelaro, and J. G. Kim, 2014: Inclusion of Linearized Moist
748 Physics in NASAs Goddard Earth Observing System Data Assimilation Tools. *Mon.*
749 *Weather Rev.*, **142**, 414-433.

750 Holdaway, D., R. M. Errico, R. Gelaro, J. G. Kim, and R. B. Mahajan, 2015: A Linearized
751 Prognostic Cloud Scheme in NASAs Goddard Earth Observing System Data Assimilation
752 Tools. *Mon. Wea. Rev.*, **143**, 4198-4219.

753 Joo, S., J. Eyre, and R. Marriott, 2013: The impact of MetOp and other satellite data within the
754 Met Office Global NWP System using and adjoint-based sensitivity method. *Mon. Wea.*
755 *Rev.*, **141**, 3331-3342.

756 Lazarus, S. M., M. E. Splitt, M. D. Lueken, and B. T. Zavodsky, 2010: Evaluation of data reduction
757 algorithms for real-time analysis. *Wea. Forecasting*, **25**, 837-851.

758 Le Marshall, J., and co-authors, 2006: Improving global analysis and forecasting with AIRS. *Bull.*
759 *Am. Meteorol. Soc.*, **87**, 891894, doi:10.1175/BAMS-87-7-891.

760 Lin, S.-J., 2004: A vertically Lagrangian finite-volume dynamical core for global models. *Mon.*
761 *Wea. Rev.*, **132**, 22932307.

762 Liu, Z.-Q. and Rabier, F., 2002: The interaction between model resolution, observation resolution
763 and observation density in data assimilation: A one-dimensional study. *Q.J.R. Meteorol.*
764 *Soc.*, **128**, 13671386.

765 —, and —, 2003: The potential of high-density observations for numerical weather predic-
766 tion: A study with simulated observations. *Q.J.R. Meteorol. Soc.*, **129**, 30133035.
767 doi:10.1256/qj.02.170

768 Lorenz, E. N., and K. A. Emanuel, 1998: Optimal sites for supplementary weather observations:
769 Simulation with a small model. *J. Atmos. Sci.*, **55**, 399414.

770 McCarty, W., G. Jedlovec, and T. L. Miller, 2009: Impact of the assimilation of
771 Atmospheric Infrared Sounder radiance measurements on short-term weather
772 forecasts. *J. Geophys. Res.*, **114**, D18122, doi:10.1029/2008JD011626.
773 <http://onlinelibrary.wiley.com/doi/10.1029/2008JD011626/full>

774 —, W., and Coauthors, 2016: MERRA-2 Input Observations: Summary and Assessment. NASA
775 Technical Report Series on Global Modeling and Data Assimilation, NASA/TM-2016-
776 104606, Vol. **46**, 61 pp. [Available online at: <https://gmao.gsfc.nasa.gov/pubs/>.]

777 McNally, A. P., Watts, P. D., A. Smith, J., Engelen, R., Kelly, G. A., Thépaut, J. N. and Matricardi,
778 M., 2006: The assimilation of AIRS radiance data at ECMWF. *Q.J.R. Meteorol. Soc.*, **132**,
779 935957. doi:10.1256/qj.04.171

780 Molod, A., L. Takacs, M. Suarez, J. Bacmeister, I.-S. Song, and A. Eichmann,
781 2012. *The GEOS-5 Atmospheric General Circulation Model: Mean Climate*
782 *and Development from MERRA to Fortuna*. NASA Technical Report Series on

Global Modeling and Data Assimilation, Vol **28**, 124p. [Available online at:

https://gmao.gsfc.nasa.gov/GEOS_systems/geos5/index_pubs.php.]

Morss, R. E., K. A. Emanuel, and C. Snyder, 2001: Idealized adaptive observation strategies for improving numerical weather prediction. *J. Atmos. Sci.*, **58**, 210232.

Ochotta, T., C. Cebhardt, D. Saupe, and W. Wergen, 2005: Adaptive thinning of atmospheric observations in data assimilation with vector quantization and filtering methods. *Q. J. R. Meteorol. Soc.*, **131**, 3427-3437.

—, —, V. Bondarenko, D. Saupe, and W. Wergen, 2007: On thinning methods for data assimilation of satellite observations. Preprints, *23rd Int. Conf. on Interactive Information Processing Systems (IIPS)*, San Antonio, TX, Amer. Meteor. Soc., 2B.3. [Available online at <http://ams.confex.com/ams/pdfpapers/118511.pdf>].

Pangaud, T., N. Fourrie, V. Guidard, M. Dahoui, and F. Rabier, 2009: Assimilation of AIRS radiances affected by mid- to low-level clouds. *Mon. Weather Rev.*, **137**, 42764292.

Purser R. J., W. Wu, D. F. Parrish, N. M. Roberts, 2003a: Numerical aspects of the application of recursive filters to variational statistical analysis. Part I: spatially homogeneous and isotropic Gaussian covariances. *Mon. Weather Rev.*, **131**, 15241535.

—, —, —, —, 2003b: Numerical aspects of the application of recursive filters to variational statistical analysis. Part II: spatially inhomogeneous and anisotropic Gaussian covariances. *Mon. Weather Rev.*, **131**, 15361548.

Putman, W. M., and S.-J. Lin, 2007: Finite-volume transport on various cubed-sphere grids. *J. Comp. Phys.*, **227** (2007), 55-78.

Rabier, F., Gauthier, P., Cardinali, C., Langland, R., Tsyrlunikov, M., Lorenc, A., Steinle, P., Gelaro, R., and Koizumi, K.: An update on THORPEX-related research in data

assimilation and observing strategies, 2008: *Nonlin. Processes Geophys.*, **15**, 81-94,
doi:10.5194/npg-15-81-2008.

Reale, O., J. Susskind, R. Rosenberg, E. Brin, E. Liu, L. P. Riishojgaard, J. Terry, J. C.
Jusem, 2008: Improving forecast skill by assimilation of quality-controlled AIRS tem-
perature retrievals under partially cloudy conditions. *Geophys. Res. Lett.*, **35**, L08809,
doi:10.1029/2007GL033002.

—, W. K. Lau, K.-M. Kim, E. Brin, 2009a: Atlantic tropical cyclogenetic processes during SOP-3
NAMMA in the GEOS-5 global data assimilation and forecast system. *J. Atmos. Sci.*, **66**,
3563-3578.

—, W. K. Lau, J. Susskind, E. Brin, E. Liu, L. P. Riishojgaard, M. Fuentes, R. Rosenberg,
2009b: AIRS Impact on the Analysis and Forecast Track of Tropical Cyclone Nargis in
a global data assimilation and forecasting system. *Geophys. Res. Lett.*, **36**, L06812,
doi:10.1029/2008GL037122.

—, W. K. Lau, and A. da Silva, 2011: Impact of interactive aerosol on the African Easterly Jet in
the NASA GEOS-5 global forecasting system. *Wea. Forecasting*, **26**, 504-519.

—, K. M. Lau, J. Susskind, and R. Rosenberg, 2012: AIRS Impact on Analysis and Forecast of an
Extreme Rainfall event (Indus River Valley, Pakistan, 2010) with a global data assimilation
and forecast system. *J. Geophys. Res.*, **117**, D08103, doi:10.1029/2011JD017093.

Rienecker, M. M., and Coauthors, 2008: *The GEOS-5 Data Assimilation System Documentation
of versions 5.0.1 and 5.1.0, and 5.2.0*. NASA Tech. Rep. Series on Global Modeling and
Data Assimilation, NASA/TM-2008-104606, Vol. **27**, 92 pp.

Singh, R., C. M. Kishtawal, and P. K. Pal, 2011: Use of Atmospheric Infrared Sounder clear-sky
and cloud-cleared radiances in the Weather Research and Forecasting 3D-VAR assimilation

system for mesoscale weather predictions over the Indian region, *J. Geophys. Res.*, **116**, D22116, doi:10.1029/2011JD016379.

Stewart, R. S., National Hurricane Center. Tropical Cyclone Report. Hurricane Edouard (AL062014), 11-19 September 2014. National Hurricane Center, 19 pp. [Available online at: www.nhc.noaa.gov/data/tcr/AL062014_Edouard.pdf]

Susskind, J., C. Barnet, J. Blaisdell, L. Iredell, F. Keita, L. Kouvaris, G. Molnar, and M. Chahine, 2006: Accuracy of geophysical parameters derived from Atmospheric Infrared Sounder/Advanced Microwave Sounding Unit as a function of fractional cloud cover, *J. Geophys. Res.*, **111**, D09S17, doi:10.1029/2005JD006272.

Susskind, J., 2011: Improved temperature sounding and quality control methodology using AIRS/AMSU Data: The AIRS Science Team Version 5 retrieval algorithm. *IEEE Trans. Geosci. Remote Sensing*, **49**, 883-907, doi: 10.1109/TGRS.2010.2070508.

Susskind, J., J. M. Blaisdell, and L. Iredell, 2014: Improved methodology for surface and atmospheric soundings, error estimates, and quality control procedures: the atmospheric infrared sounder science team version-6 retrieval algorithm, *J. Appl. Rem. Sens.*, **8**, 084994. <https://doi.org/10.1117/1.JRS.8.084994>

Todling, R., Gu, W., Daescu, D. N. (2015). Accounting for Satellite Radiance Inter-channel Correlations in GSI. *JCSDA Quarterly*, **52**. Available online at https://www.jcsda.noaa.gov/documents/newsletters/2015_04JCSDAQarterly.pdf

Trahan, S., and L. Sparling, 2012: An analysis of NCEP tropical cyclone vitals and potential effects on forecasting models. *Wea. Forecasting*, **27**, 744756.

Trémolet, Y., 2008: Computation of observation sensitivity and observation impact in incremental variational data assimilation. *Tellus A*, **60**, 964978.

852 Wang, P., J. Li, M. D. Goldberg, T. J. Schmit, A. H. N. Lim, Z. Li, H. Han, J. Li, and S. A. Acker-
853 man, 2015: Assimilation of thermodynamic information from advanced infrared sounders
854 under partially cloudy skies for regional NWP. *Journal of Geophysical Research: Atmo-*
855 *spheres*, **120**, (11), 54695484.

856 Wang, P., J. Li, Z. Li, A. H. N. Lim, J. Li, T. J. Schmit, and M. D. Goldberg, 2017: The impact of
857 cross-track infrared sounder (CrIS) cloud-cleared radiances on hurricane Joaquin (2015)
858 and Matthew (2016) forecasts. *Journal of Geophysical Research: Atmospheres*, **122** (24),
859 1320113218.

860 Wu W.S., R. J. Purser, D. F. Parrish, 2002: Three-dimensional variational analysis with spatially
861 inhomogeneous covariances. *Mon. Weather Rev.*, **130**, 29052916.

862 Zhou, Y., W. K. Lau, O. Reale, R. Rosenberg, 2010: AIRS Impact on precipitation analysis and
863 forecast of tropical cyclones in a global data assimilation and forecasting system. *Geophys.*
864 *Res. Letters*, **37**, L02806, doi.1029/2009GL041494.

865 Zhu, T., and S. Boukabara, 2015: Development and impact study of community
866 satellite data thinning and representation optimization tool. 95th AMS An-
867 nual Meeting, January 04-08, 2015, Phoenix, Arizona [Available online at
868 <https://ams.confex.com/ams/95Annual/webprogram/Paper267375.html>].

869 Zhu Y., E. Liu, R. Mahajan, C. Thomas, D. Groff, P. Van Delst, A. Collard, D. Kleist, R. Treadon, J.
870 C. Derber, 2016: All-sky microwave radiance assimilation in NCEP's GSI analysis system.
871 *Mon. Wea. Rev.*, **144**, 47094735.

873 **Table 1.** Thinning experiments setup, clear-sky radiances. The horizontal line separate
874 OPS, RAD, RAD2 and RAD3 (global thinning experiments), from the adap-
875 tive experiments. First column: experiment names; second column: size of the
876 thinning box adopted globally; third column: size of the TC-centered, mov-
877 ing domain, in which a denser thinning is adopted; fourth column: thinning
878 box size inside the TC domain; fifth column: density of AIRS radiances as-
879 similated globally compared to the reference x in the RAD experiment; sixth
880 column: density of AIRS radiances assimilated inside the TC domain, com-
881 pared to RAD. Among the five adaptive thinning experiments, SThin combines
882 the data density of RAD3 and RAD2 and have been determined to be the best
883 of the five. The experiment settings for SThin2, SThin3, SThin4 and SThin5
884 are listed for completeness. In all the experiments except OPS the vortex relo-
885 cator is disabled so as to give AIRS data the possibility to constrain the storm
886 position. 42

887 **Table 2.** Adaptive thinning experiments setup, cloud-cleared radiances. First column:
888 experiment names; second column: size of the thinning box adopted globally;
889 third column: size of the TC-centered, moving domain, in which a denser thin-
890 ning is adopted; fourth column: thinning box size inside the TC domain; fifth
891 column: density of AIRS radiances assimilated globally compared to the ref-
892 erence x in the CLD (and RAD) experiment; sixth column: density of AIRS
893 radiances assimilated inside the TC domain, compared to CLD. In all the ex-
894 periments the vortex relocater is disabled so as to give AIRS data the possibility
895 to constrain the storm position. 43

Clear-sky Experiments

Exp Name	Global	TC	TC Domain	Global	TC Domain
	Thin Box	Domain	Thin Box	Density	Density
OPS	145	-	-	x	-
RAD	145	-	-	x	-
RAD2	75	-	-	$\sim 4x$	-
RAD3	300	-	-	$\sim 1/4x$	-
SThin	300	$15^\circ \times 15^\circ$	75	$\sim 1/4x$	$\sim 4x$
SThin2	300	$15^\circ \times 15^\circ$	145	$\sim 1/4x$	x
SThin3	300	$15^\circ \times 15^\circ$	110	$\sim 1/4x$	$\sim 1/2x$
SThin4	300	$7.5^\circ \times 7.5^\circ$	75	$\sim 1/4x$	$\sim 4x$
SThin5	300	$30^\circ \times 30^\circ$	75	$\sim 1/4x$	$\sim 4x$

TABLE 1. Thinning experiments setup, clear-sky radiances. The horizontal line separate OPS, RAD, RAD2 and RAD3 (global thinning experiments), from the adaptive experiments. First column: experiment names; second column: size of the thinning box adopted globally; third column: size of the TC-centered, moving domain, in which a denser thinning is adopted; fourth column: thinning box size inside the TC domain; fifth column: density of AIRS radiances assimilated globally compared to the reference x in the RAD experiment; sixth column: density of AIRS radiances assimilated inside the TC domain, compared to RAD. Among the five adaptive thinning experiments, SThin combines the data density of RAD3 and RAD2 and have been determined to be the best of the five. The experiment settings for SThin2, SThin3, SThin4 and SThin5 are listed for completeness. In all the experiments except OPS the vortex relocater is disabled so as to give AIRS data the possibility to constrain the storm position.

Cloud-Cleared Experiments

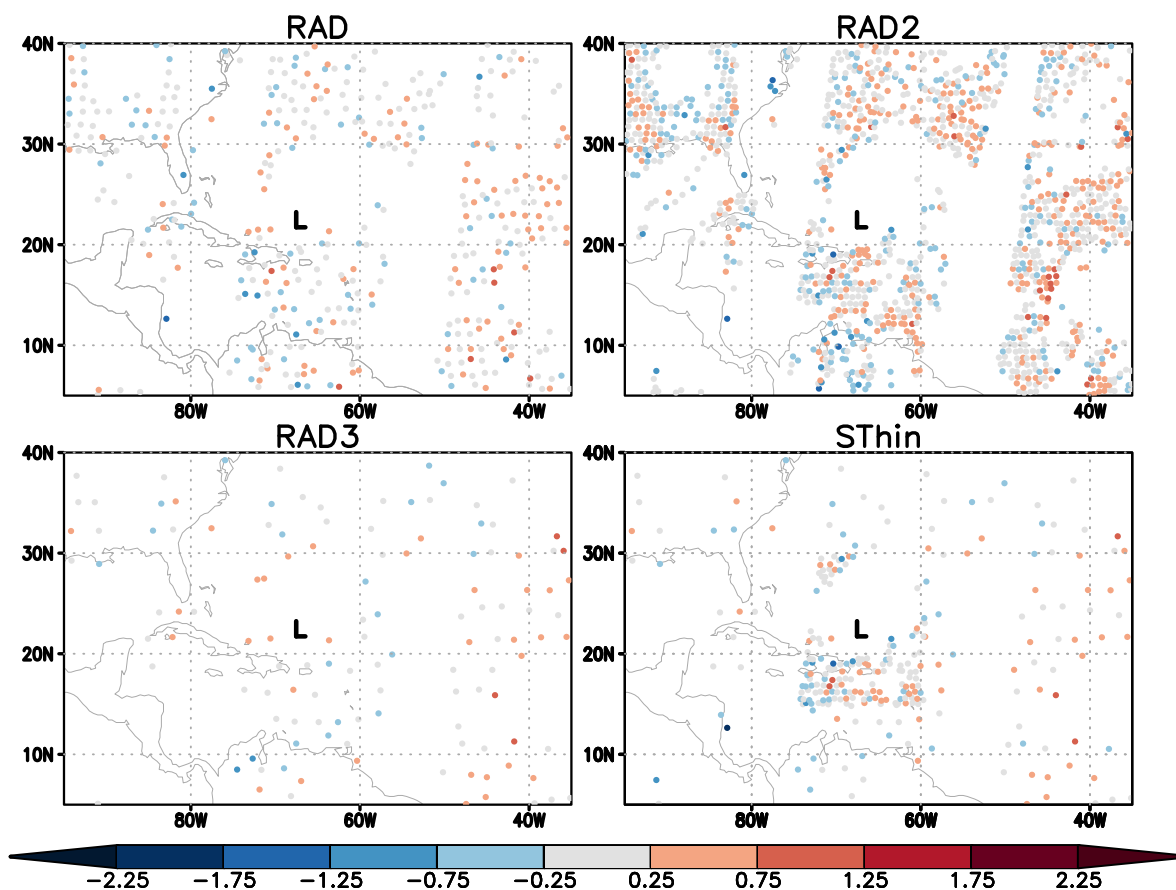
Exp Name	Global	TC	TC Domain	Global	TC Domain
	Thin Box	Domain	Thin Box	Density	Density
CLD	145	-	-	x	-
CLD2	75	-	-	$\sim 4x$	-
CLD3	300	-	-	$\sim 1/4x$	-
SThin_CLD	300	$15^\circ \times 15^\circ$	75	$\sim 1/4x$	$\sim 4x$
SThin2_CLD	300	$15^\circ \times 15^\circ$	145	$\sim 1/4x$	x

TABLE 2. Adaptive thinning experiments setup, cloud-cleared radiances. First column: experiment names; second column: size of the thinning box adopted globally; third column: size of the TC-centered, moving domain, in which a denser thinning is adopted; fourth column: thinning box size inside the TC domain; fifth column: density of AIRS radiances assimilated globally compared to the reference x in the CLD (and RAD) experiment; sixth column: density of AIRS radiances assimilated inside the TC domain, compared to CLD. In all the experiments the vortex relocater is disabled so as to give AIRS data the possibility to constrain the storm position.

LIST OF FIGURES

Fig. 1.	Clear-sky AIRS radiance coverage in all the experiments at 0600 UTC 15 October 2014. L is Hurricane Gonzalo's center, from the NHC. Circles indicate locations of assimilated radiances: observation minus forecast (O-F) brightness temperatures (values in K), channel 169, corresponding to approximately 185hPa.	45
Fig. 2.	Global anomaly correlation for AIRS clear-sky radiance assimilation experiments, computed for the forecasts initialized from September 21st to October 31st, 2014 (41 forecasts). Forecast skill as a function of forecast time (panel above), experiment minus OPS forecast skill difference (center panel), experiment minus RAD forecast skill difference (lower panel). The horizontal bars represent statistical significance.	46
Fig. 3.	Vertical profiles of Temperature RMSE for AIRS clear-sky radiance assimilation experiments. Tropics only ($30^{\circ}S$ to $30^{\circ}N$). All the RMSE profiles for experiments with adaptive thinning are contained between the RAD2 and RAD3 (not shown for clarity).	47
Fig. 4.	Above: Zonal vertical section of wind (ms^{-1}), temperature ($^{\circ}C$, solid black contours) and temperature anomaly (solid red contours, contours every $2^{\circ}C$, only $\geq 4^{\circ}C$ for clarity) for Hurricane Gonzalo at 1200 UTC 16 October 2014, comparing the RAD, RAD3 and SThin experiments. Below: horizontal winds at 850 hPa (ms^{-1} , shaded) and slp (hPa, solid).	48
Fig. 5.	Domains for measuring the impact of AIRS observations close to Gonzalo using the adjoint based FSOI. The inner domain (black lines) shows where the response function for the adjoint sensitivity is computed, i.e. the region where the impact is measured. The outer box (red lines) shows the region for which impacts are screened, AIRS observations occurring outside this region are not included in subsequent metrics. Gonzalo's track from NHC is superimposed, with colors corresponding to intensity (green=tropical depression, yellow=tropical storm, red=hurricane, purple=major hurricane); extratropical phase not plotted.	49
Fig. 6.	Fraction of observations from each instrument type that reduced 24-hour forecast error for the period 1 -31 October 2014. Red, green and blue bars show the impact on the fraction of beneficial observations produced by the RAD, RAD2, and the RAD3 experiments, respectively.	50
Fig. 7.	Fraction of observations from each instrument type that reduced 24-hour forecast error for the period 12-19 October 2014, over a domain encompassing the track and life cycle of Hurricane Gonzalo. Red, green and blue bars show the impact on the fraction of beneficial observations produced by the RAD, RAD2 and RAD3 experiment, respectively. The impacts are computed as the average of the adjoint initialized across all 0600 UTC and 1800 UTC analyses, corresponding approximately to the Aqua passes over the domain.	51
Fig. 8.	Cloud-cleared AIRS radiance coverage in all the experiments at 0600 UTC 15 October 2014. L is Hurricane Gonzalo's center, from the NHC. Circles indicate locations of assimilated radiances: observation minus forecast (O-F) brightness temperatures (values in K), channel 169, corresponding to approximately 185hPa.	52
Fig. 9.	Global anomaly correlation for AIRS cloud-cleared radiance assimilation experiments, for the forecasts initialized from September 21st to October 31st, 2014 (41 forecasts). Forecast skill as a function of forecast time (panel above), experiment minus OPS forecast skill difference (center panel), experiment minus RAD forecast skill difference (lower panel). The horizontal bars represent statistical significance.	53

956	Fig. 10.	Analysis of minimum center pressure for Hurricane Edouard in RAD, CLD3, and	
957		SThin2_CLD experiments, compared to the observations (National Hurricane Center Best	
958		Track).	54
959	Fig. 11.	Above: Zonal vertical section of wind (ms^{-1}), temperature ($^{\circ}C$, solid black contours)	
960		and temperature anomaly (solid red contours, contours every $2^{\circ}C$, only $\geq 4^{\circ}C$ for clar-	
961		ity) for Hurricane Edouard at 1800 UTC 17 September 2014, comparing the RAD, CLD	
962		and SThin2-CLD experiments. Below: horizontal winds at 850 hPa (ms^{-1} , shaded) and slp	
963		(hPa, solid).	55
964	Fig. 12.	Analysis of minimum center pressure for Hurricane Gonzalo in RAD, CLD3, and	
965		SThin2_CLD experiments, compared to the observations (National Hurricane Center Best	
966		Track).	56
967	Fig. 13.	Same as Fig ??, but for Hurricane Gonzalo at 1800 UTC 16 October 2014.	57
968	Fig. 14.	Analysis of minimum center pressure for Hurricane Vance in RAD, CLD3 and SThin2_CLD	
969		experiments, compared to the observations (National Hurricane Center Best Track).	58
970	Fig. 15.	Same as Fig ??, but for Hurricane Vance at 1200 UTC 03 November 2014. Red contours	
971		$\geq 2^{\circ}C$	59
972	Fig. 16.	RMS Error for center pressure forecast (hPa) as a function of forecast time. Gonzalo (top),	
973		Vance (bottom).	60
974	Fig. 17.	Fraction of observations from each instrument type that reduced 24-hour forecast error for	
975		the period 1-31 October 2014. Red, blue and yellow bars show the impact on the fraction	
976		of beneficial observations produced by the CLD, CLD3, and the SThin2_CLD experiment,	
977		respectively.	61
978	Fig. 18.	Fraction of observations from each instrument type that reduced 24-hour forecast error for	
979		the period 12-19 October 2014, over a domain encompassing the track and life cycle of	
980		Hurricane Gonzalo. Red, blue and yellow bars show the impact on the fraction of beneficial	
981		observations produced by the CLD, CLD3, and the SThin2_CLD experiment, respectively	
982		(averaging the forecasts initialized at 0600 UTC and 1800 UTC).	62



983 FIG. 1. Clear-sky AIRS radiance coverage in all the experiments at 0600 UTC 15 October 2014. **L** is Hur-
 984 ricane Gonzalo's center, from the NHC. Circles indicate locations of assimilated radiances: observation minus
 985 forecast (O-F) brightness temperatures (values in K), channel 169, corresponding to approximately 185hPa.

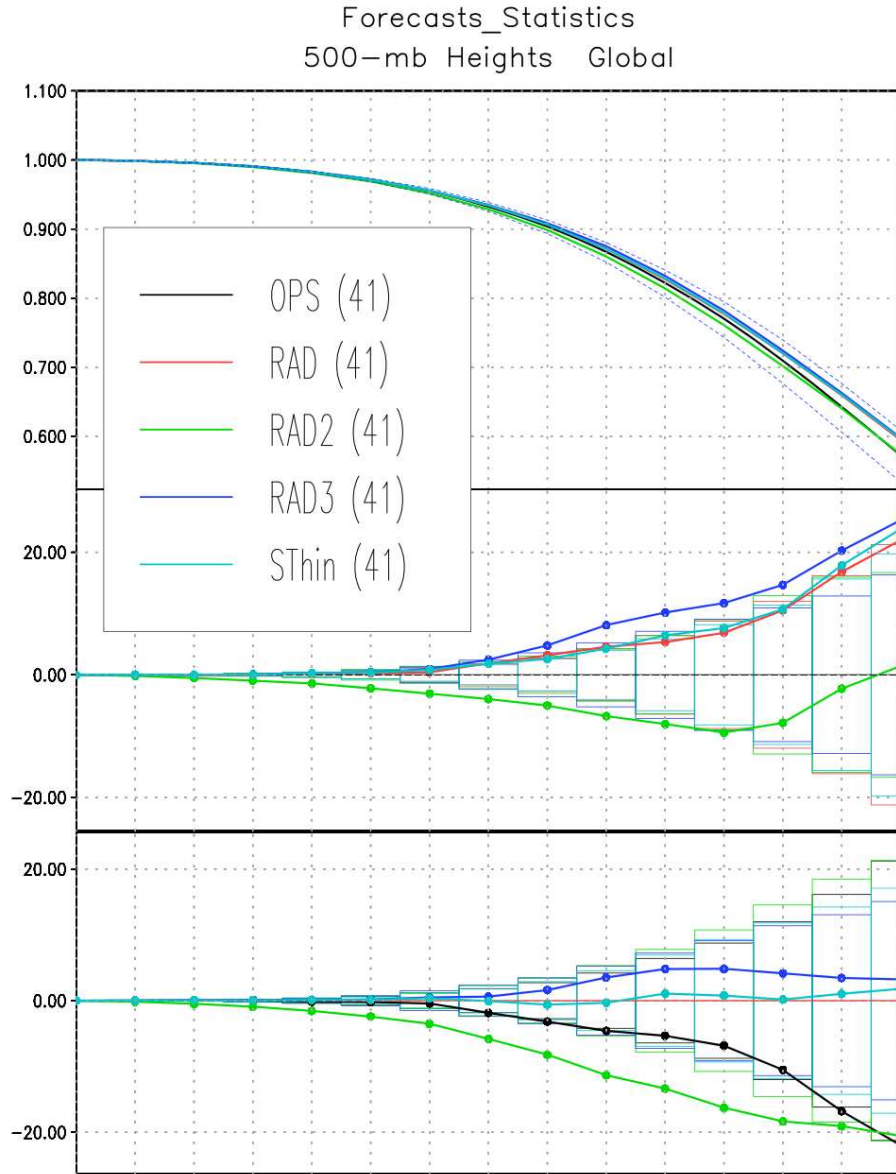


FIG. 2. Global anomaly correlation for AIRS clear-sky radiance assimilation experiments, computed for the forecasts initialized from September 21st to October 31st, 2014 (41 forecasts). Forecast skill as a function of forecast time (panel above), experiment minus OPS forecast skill difference (center panel), experiment minus RAD forecast skill difference (lower panel). The horizontal bars represent statistical significance.

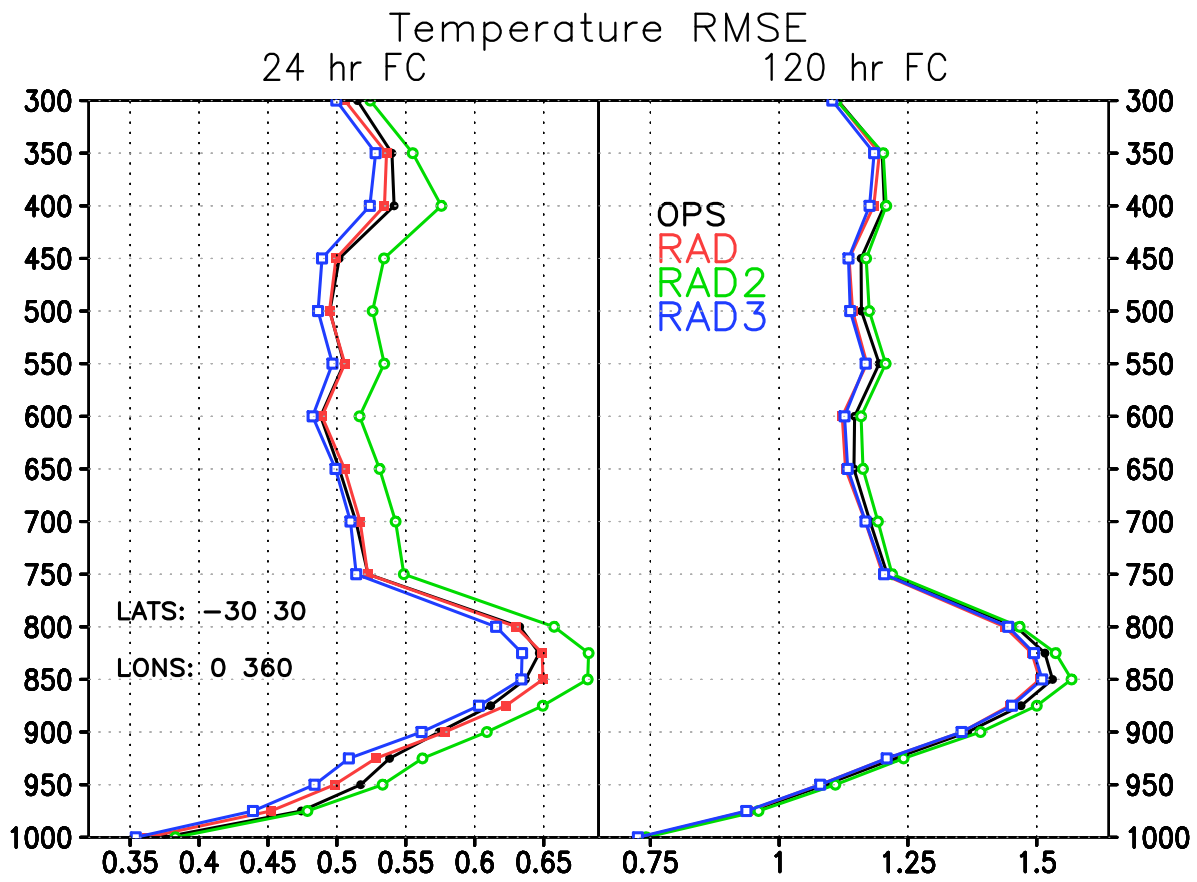


FIG. 3. Vertical profiles of Temperature RMSE for AIRS clear-sky radiance assimilation experiments. Tropics only ($30^{\circ}S$ to $30^{\circ}N$). All the RMSE profiles for experiments with adaptive thinning are contained between the RAD2 and RAD3 (not shown for clarity).

Gonzalo 12Z16OCT2014

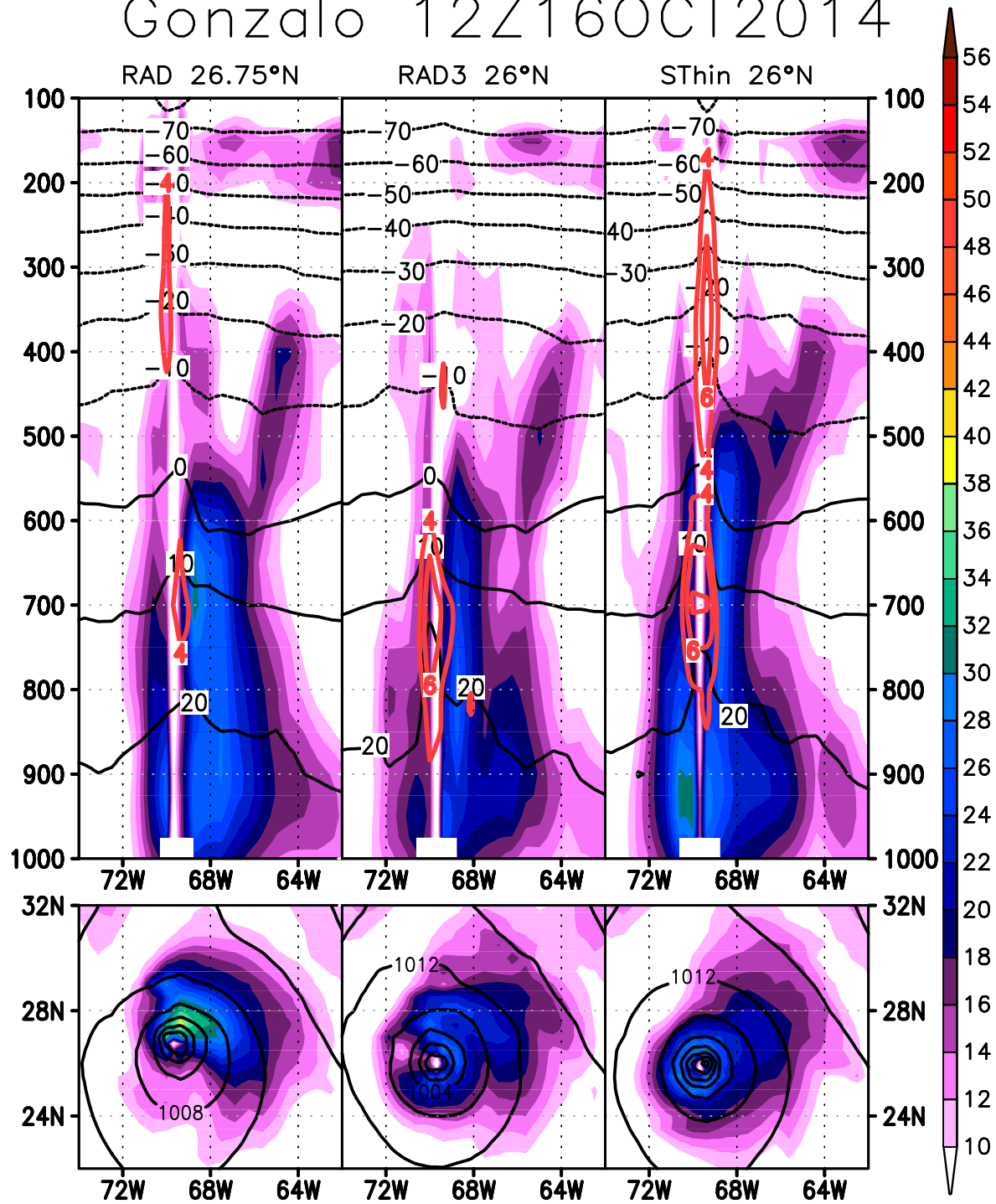


FIG. 4. Above: Zonal vertical section of wind ($m s^{-1}$), temperature ($^{\circ}C$, solid black contours) and temperature anomaly (solid red contours, contours every $2^{\circ}C$, only $\geq 4^{\circ}C$ for clarity) for Hurricane Gonzalo at 1200 UTC 16 October 2014, comparing the RAD, RAD3 and SThin experiments. Below: horizontal winds at 850 hPa ($m s^{-1}$, shaded) and slp (hPa, solid).

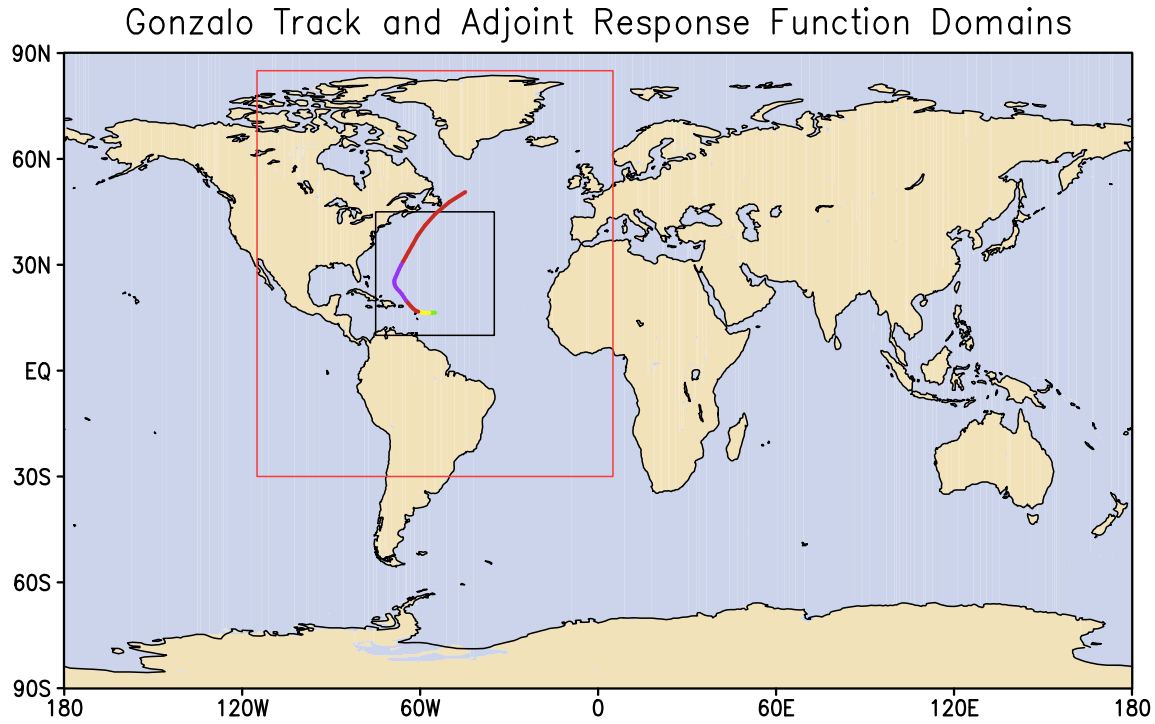


FIG. 5. Domains for measuring the impact of AIRS observations close to Gonzalo using the adjoint based FSOI. The inner domain (black lines) shows where the response function for the adjoint sensitivity is computed, i.e. the region where the impact is measured. The outer box (red lines) shows the region for which impacts are screened, AIRS observations occurring outside this region are not included in subsequent metrics. Gonzalo's track from NHC is superimposed, with colors corresponding to intensity (green=tropical depression, yellow=tropical storm, red=hurricane, purple=major hurricane); extratropical phase not plotted.

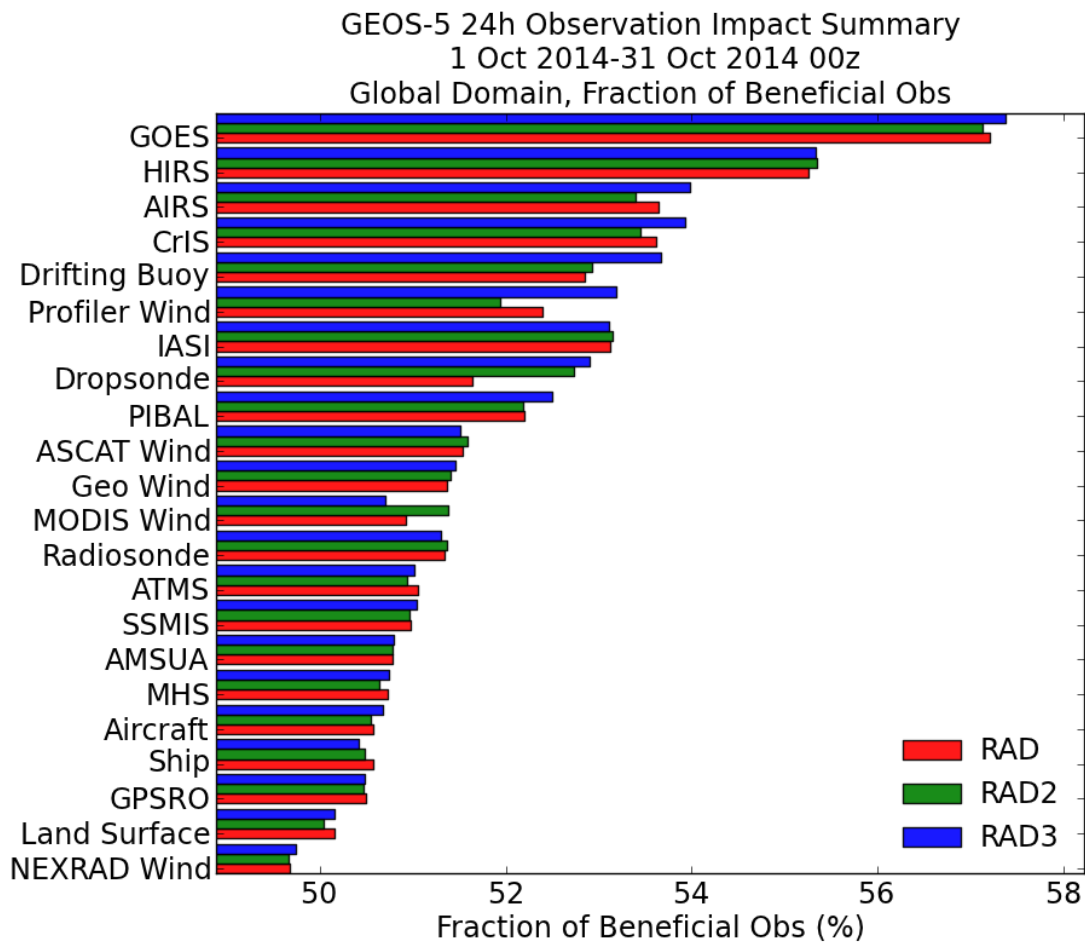
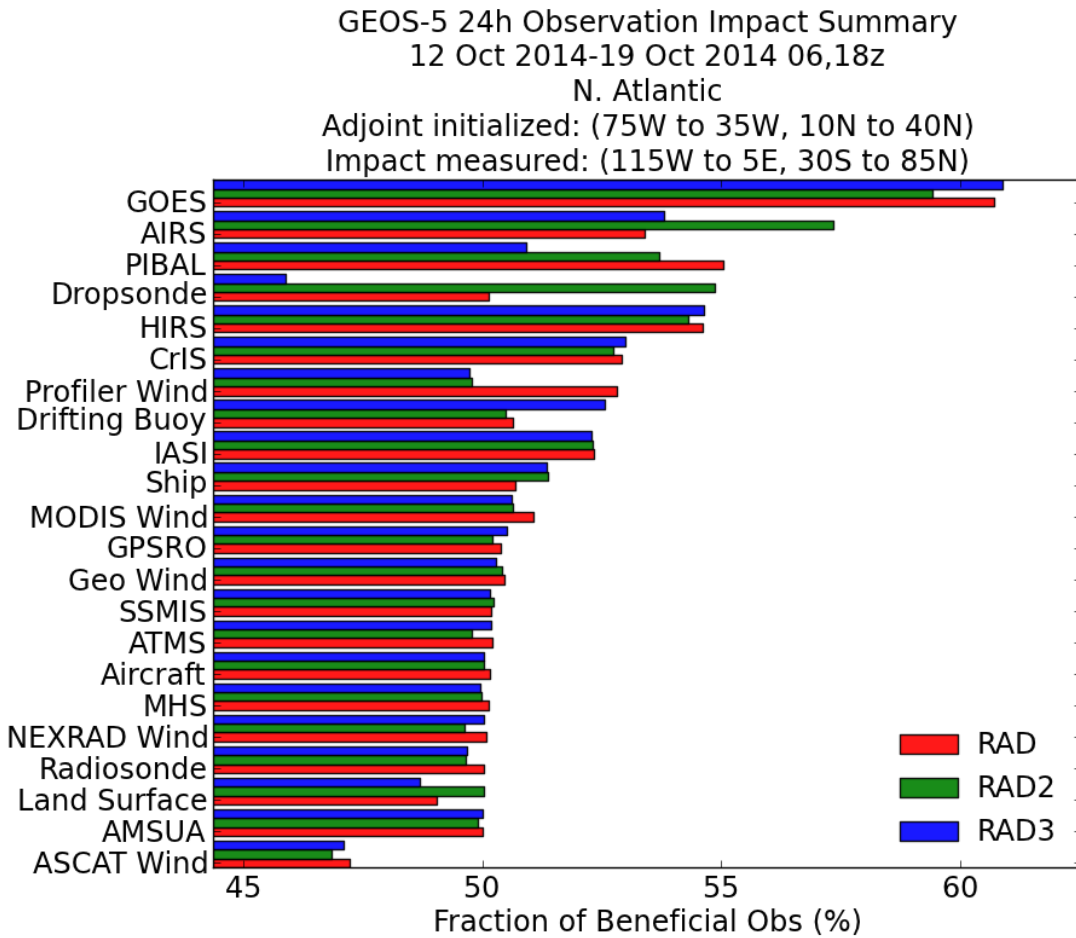


FIG. 6. Fraction of observations from each instrument type that reduced 24-hour forecast error for the period 1
-31 October 2014. Red, green and blue bars show the impact on the fraction of beneficial observations produced
by the RAD, RAD2, and the RAD3 experiments, respectively.



1006 FIG. 7. Fraction of observations from each instrument type that reduced 24-hour forecast error for the period
 1007 12-19 October 2014, over a domain encompassing the track and life cycle of Hurricane Gonzalo. Red, green and
 1008 blue bars show the impact on the fraction of beneficial observations produced by the RAD, RAD2 and RAD3
 1009 experiment, respectively. The impacts are computed as the average of the adjoint initialized across all 0600 UTC
 1010 and 1800 UTC analyses, corresponding approximately to the Aqua passes over the domain.

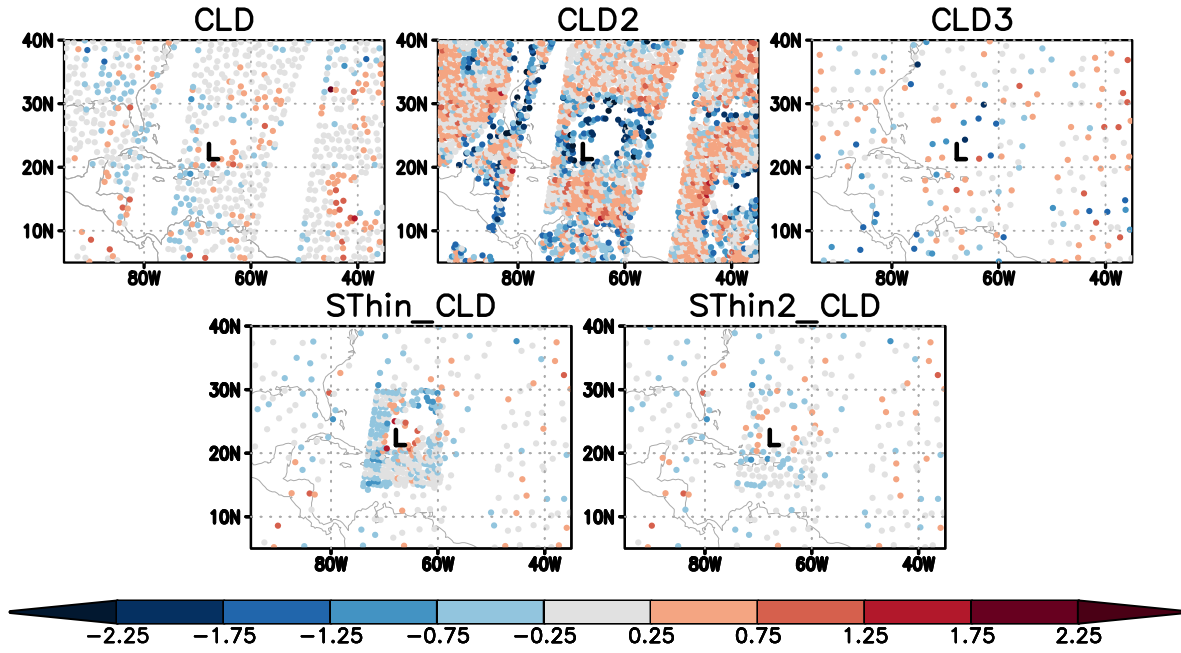


FIG. 8. Cloud-cleared AIRS radiance coverage in all the experiments at 0600 UTC 15 October 2014. **L** is Hurricane Gonzalo's center, from the NHC. Circles indicate locations of assimilated radiances: observation minus forecast (O-F) brightness temperatures (values in K), channel 169, corresponding to approximately 185hPa.

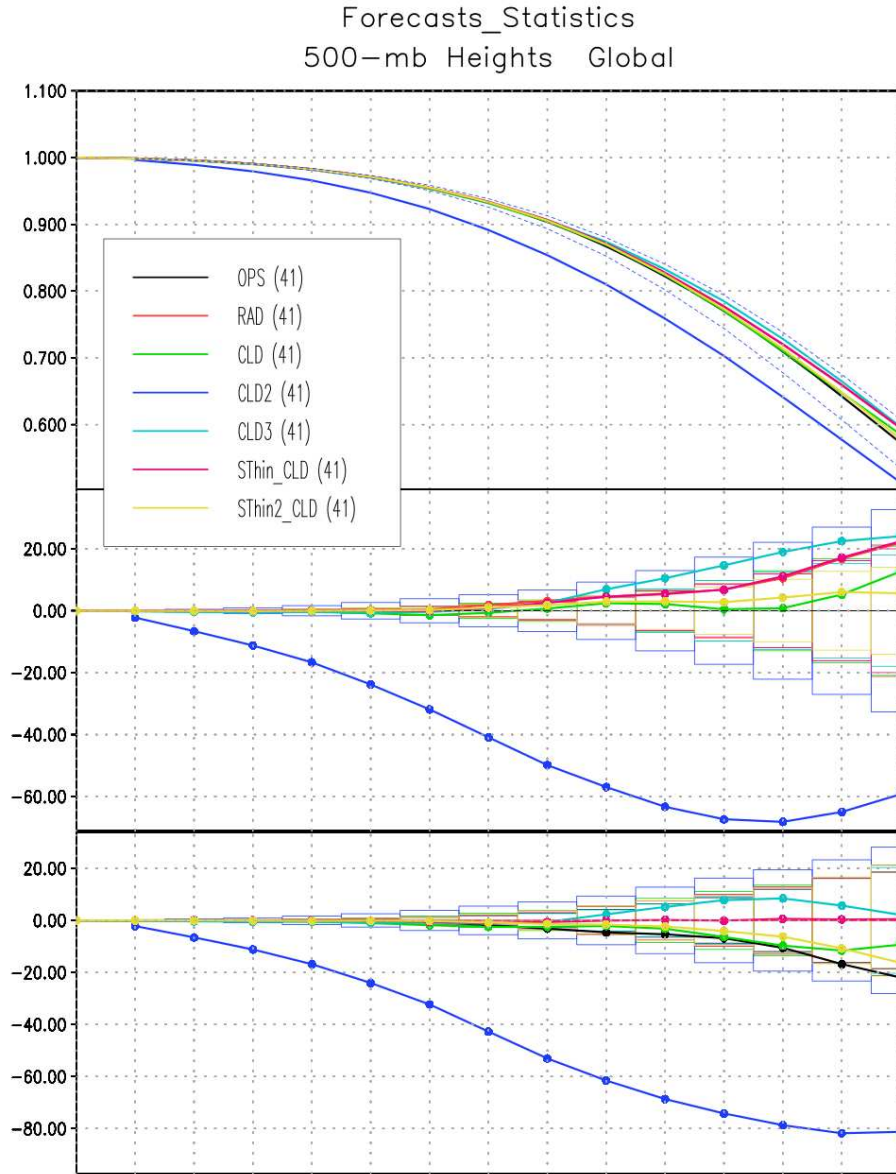


FIG. 9. Global anomaly correlation for AIRS cloud-cleared radiance assimilation experiments, for the forecasts initialized from September 21st to October 31st, 2014 (41 forecasts). Forecast skill as a function of forecast time (panel above), experiment minus OPS forecast skill difference (center panel), experiment minus RAD forecast skill difference (lower panel). The horizontal bars represent statistical significance.

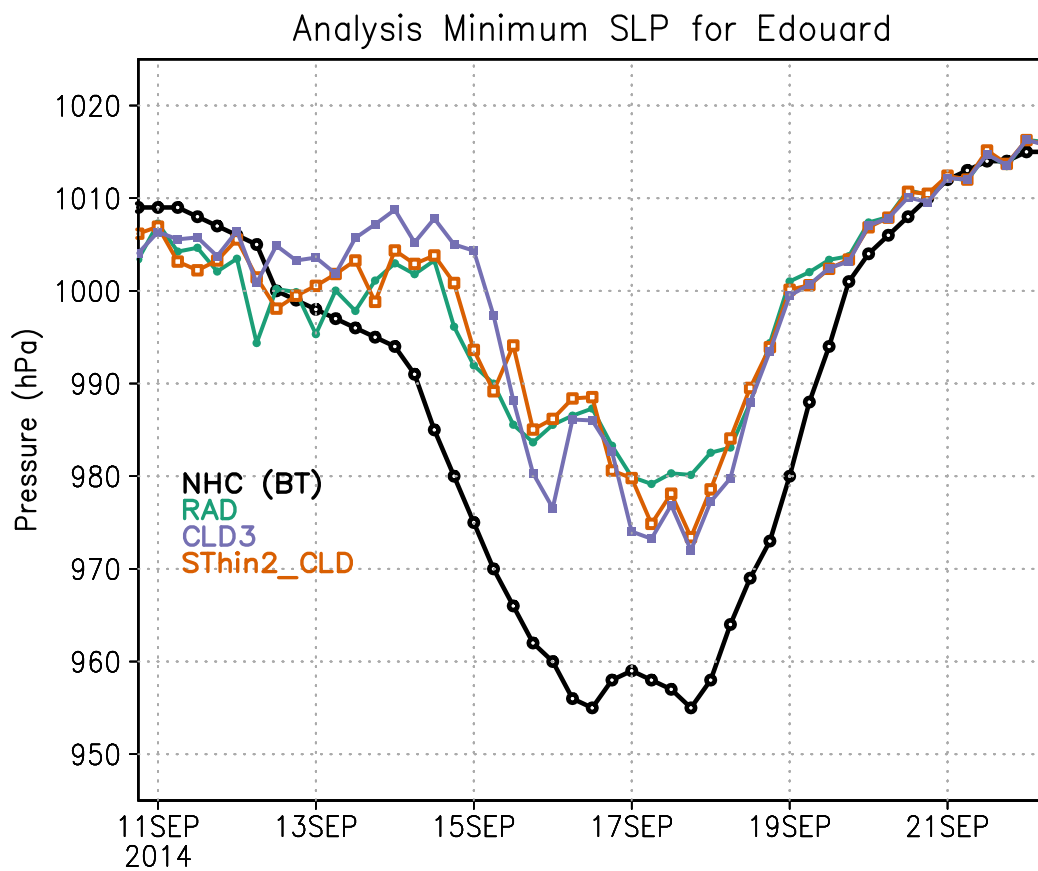


FIG. 10. Analysis of minimum center pressure for Hurricane Edouard in RAD, CLD3, and SThin2_CLD experiments, compared to the observations (National Hurricane Center Best Track).

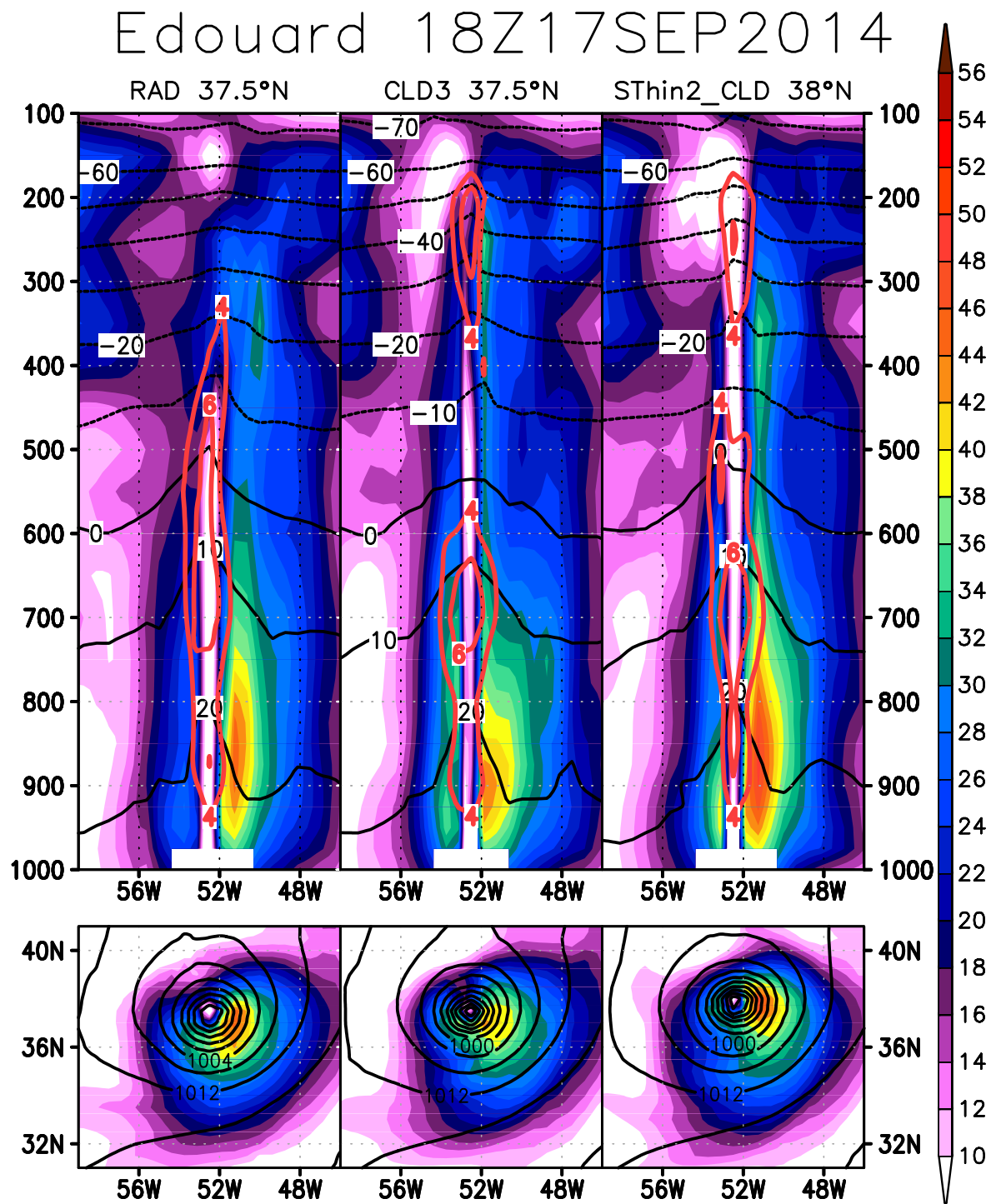


FIG. 11. Above: Zonal vertical section of wind ($m s^{-1}$), temperature ($^{\circ}C$, solid black contours) and temperature anomaly (solid red contours, contours every $2^{\circ}C$, only $\geq 4^{\circ}C$ for clarity) for Hurricane Edouard at 1800 UTC 17 September 2014, comparing the RAD, CLD and SThin2-CLD experiments. Below: horizontal winds at 850 hPa ($m s^{-1}$, shaded) and slp (hPa, solid).

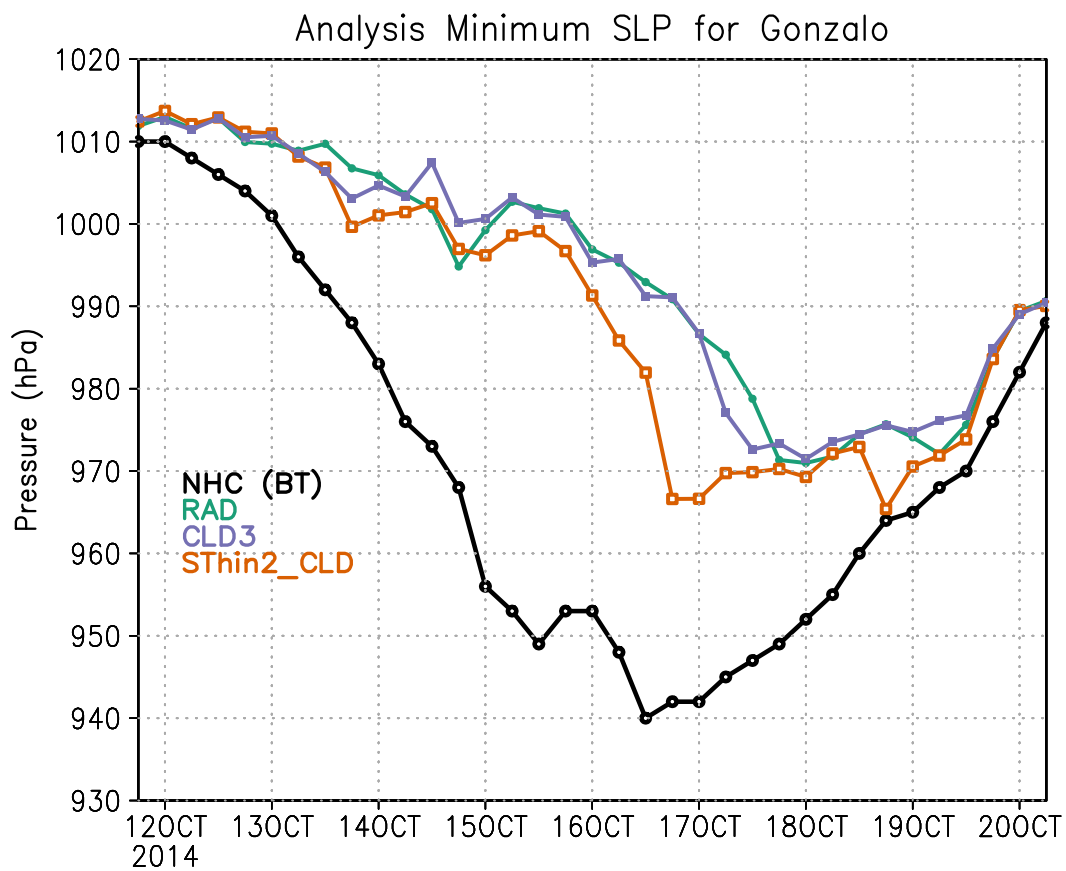


FIG. 12. Analysis of minimum center pressure for Hurricane Gonzalo in RAD, CLD3, and SThin2_CLD experiments, compared to the observations (National Hurricane Center Best Track).

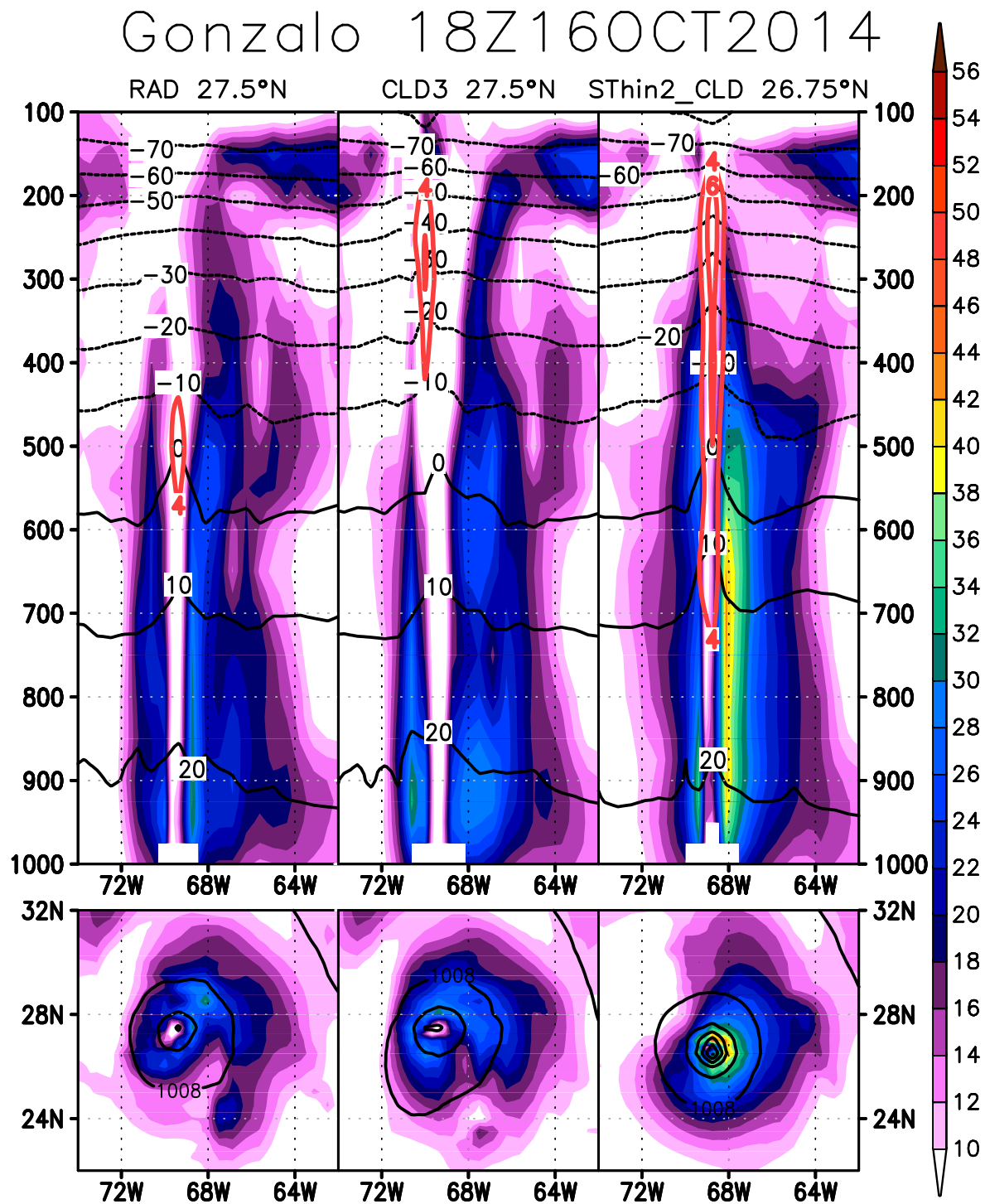


FIG. 13. Same as Fig 11, but for Hurricane Gonzalo at 1800 UTC 16 October 2014.

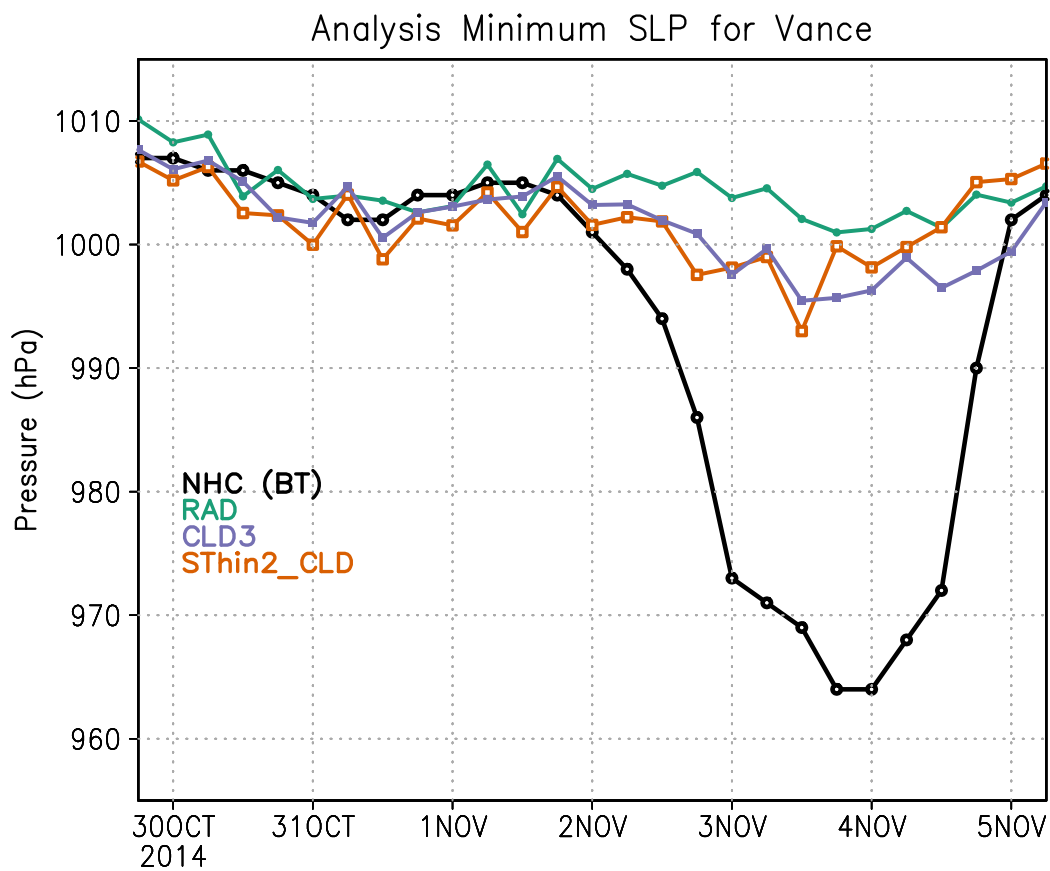


FIG. 14. Analysis of minimum center pressure for Hurricane Vance in RAD, CLD3 and SThin2_CLD experiments, compared to the observations (National Hurricane Center Best Track).

Vance 12Z03NOV2014

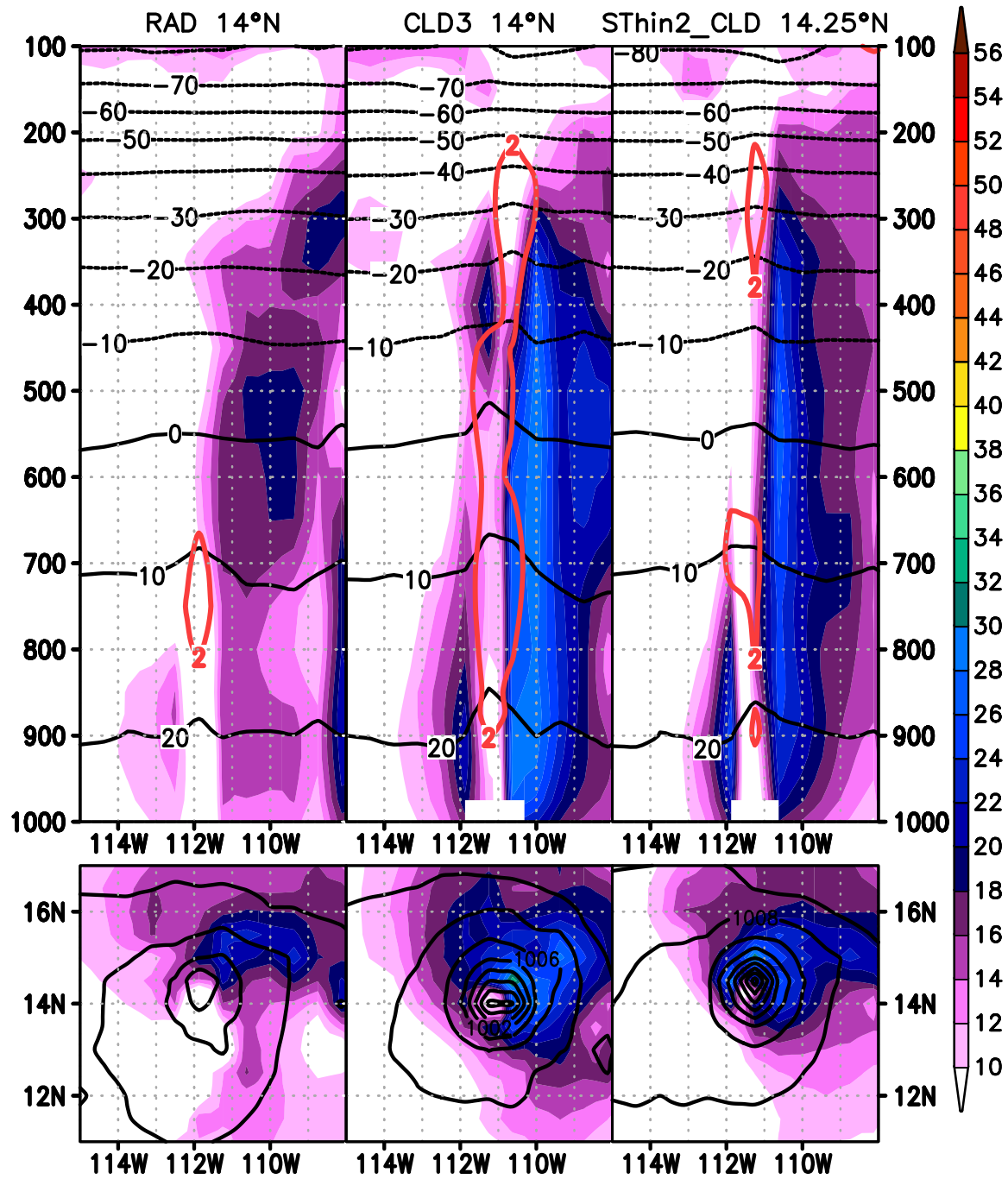


FIG. 15. Same as Fig 11, but for Hurricane Vance at 1200 UTC 03 November 2014. Red contours $\geq 2^\circ\text{C}$

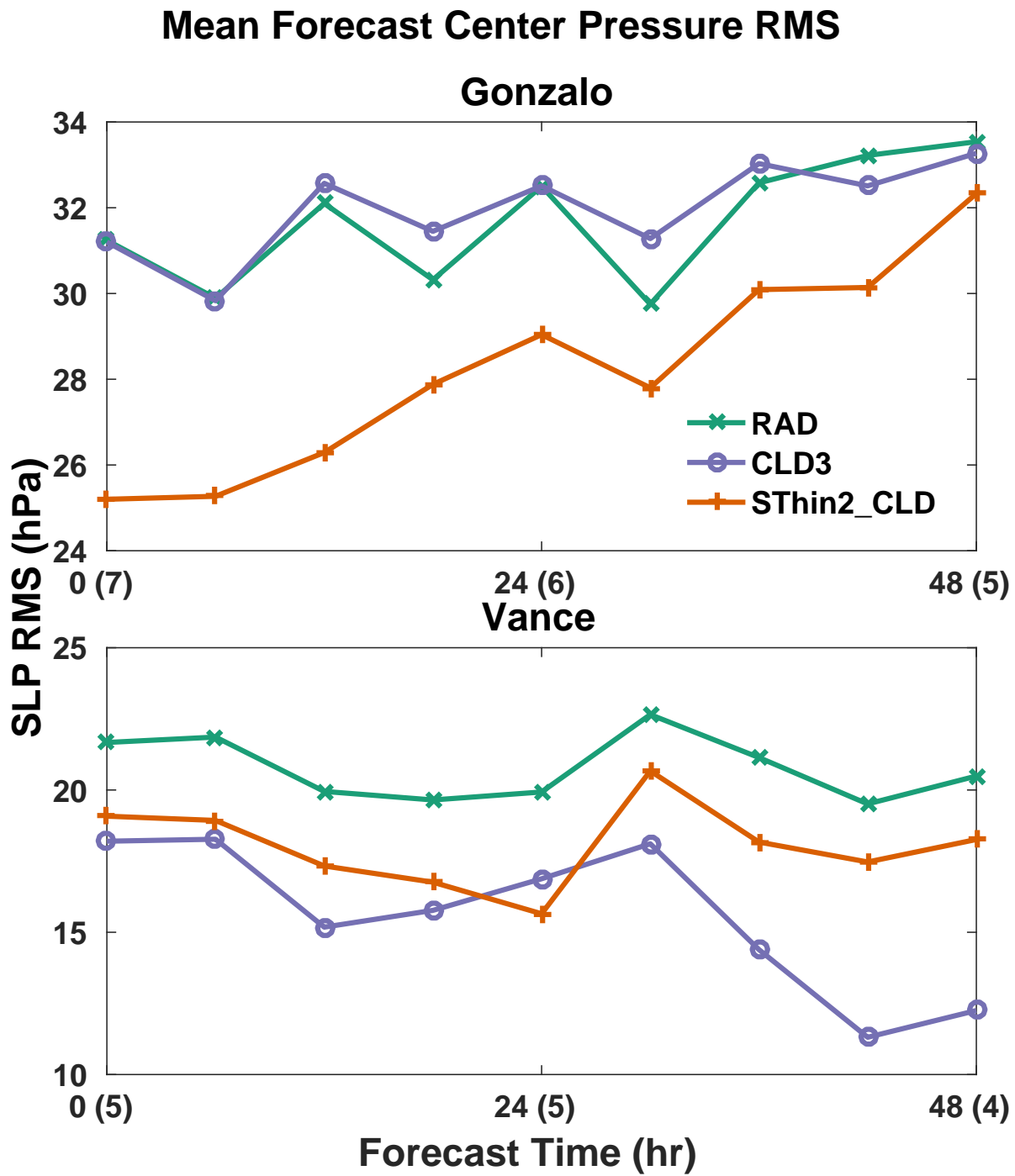


FIG. 16. RMS Error for center pressure forecast (hPa) as a function of forecast time. Gonzalo (top), Vance (bottom).

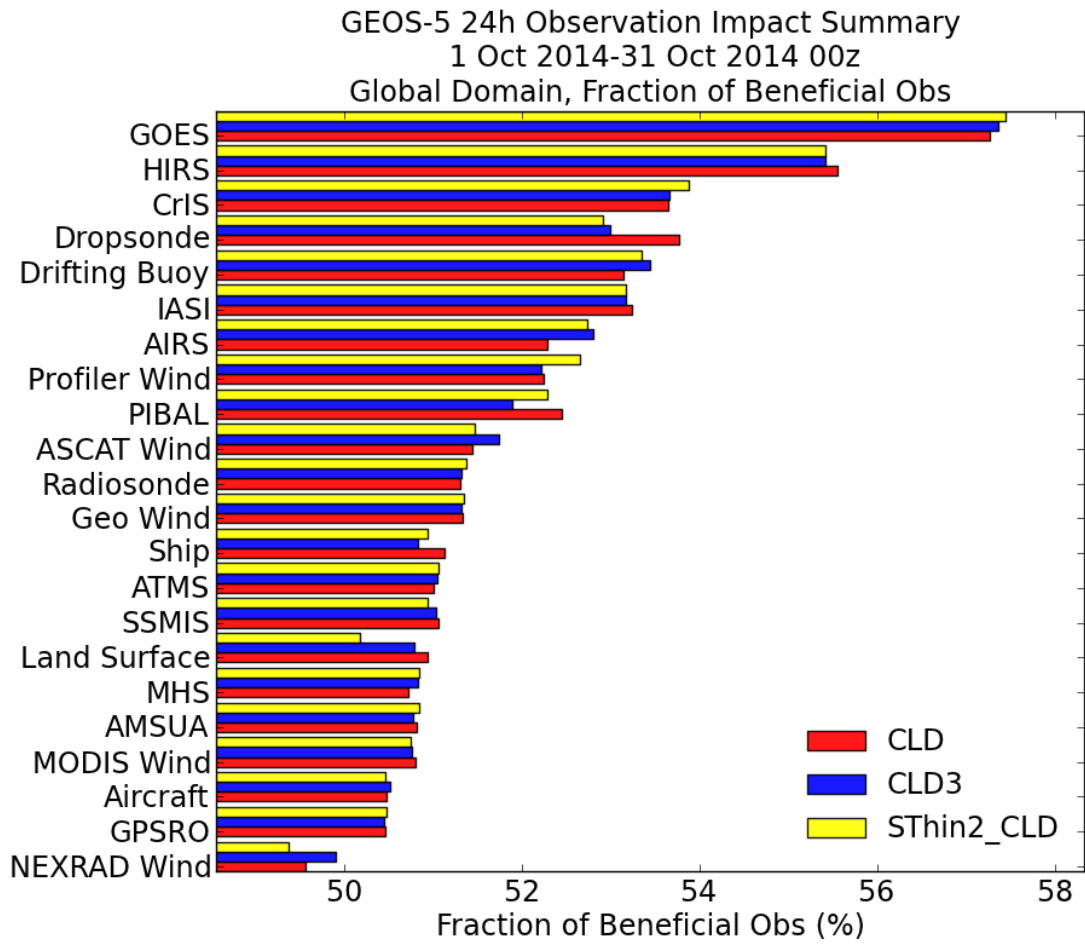


FIG. 17. Fraction of observations from each instrument type that reduced 24-hour forecast error for the period 1-31 October 2014. Red, blue and yellow bars show the impact on the fraction of beneficial observations produced by the CLD, CLD3, and the SThin2_CLD experiment, respectively.

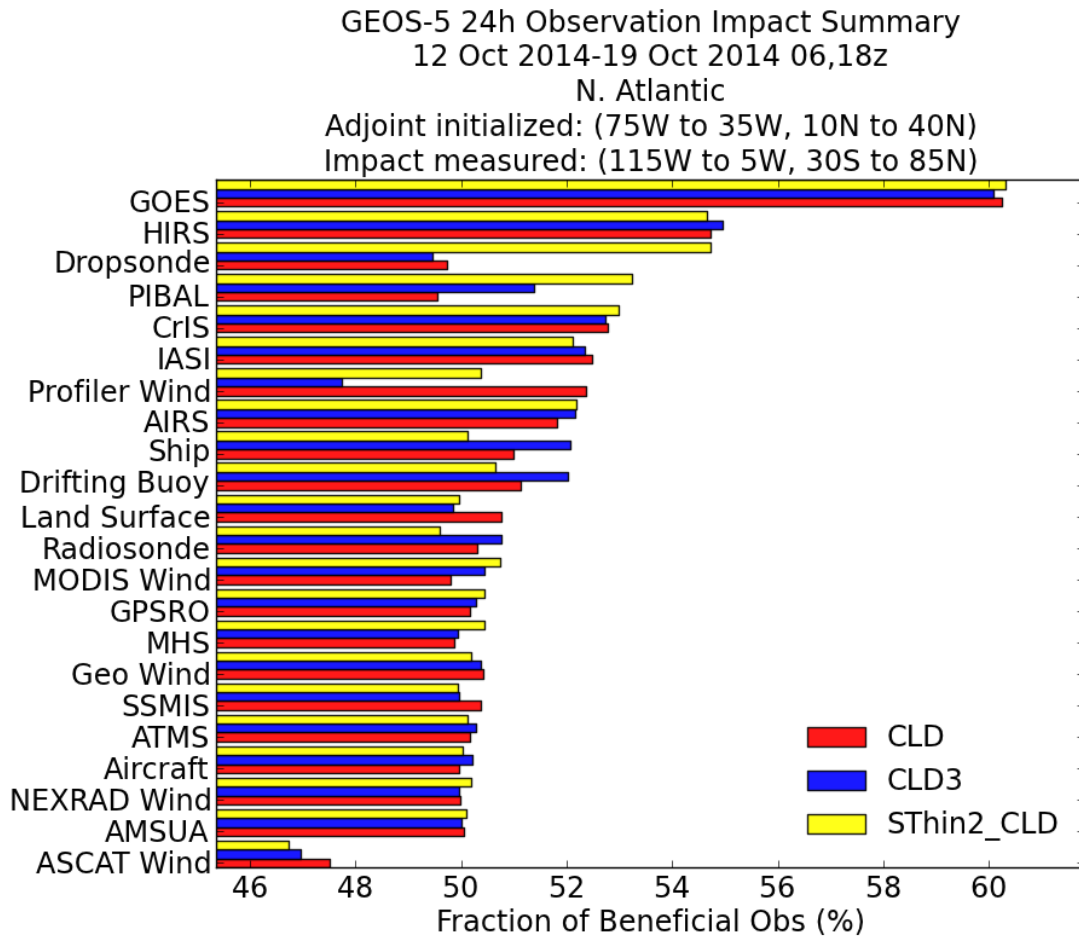


FIG. 18. Fraction of observations from each instrument type that reduced 24-hour forecast error for the period
 12-19 October 2014, over a domain encompassing the track and life cycle of Hurricane Gonzalo. Red, blue and
 yellow bars show the impact on the fraction of beneficial observations produced by the CLD, CLD3, and the
 SThin2_CLD experiment, respectively (averaging the forecasts initialized at 0600 UTC and 1800 UTC).